buildings

MDPI

Article

Finite Element Analysis of Axial Compression Behavior of L-Shaped Concrete-Filled Steel Tubular Columns with Different Combinations

Hexiao Li [1,2,3], Zhong Tao [1,3,*] and Dongji Han [1,4]

1 Faculty of Civil Engineering and Mechanics, Kunming University of Science and Technology, Kunming 650500, China; lihexiao@ynou.edu.cn (H.L.); handongji@cscec.com (D.H.)
2 College of Urban Construction, Yunnan Open University, Kunming 650223, China
3 Yunnan Earthquake Engineering Research Institute, Kunming 650000, China
4 3rd Construction Co., Ltd. of China Construction 5th Engineering Bureau, Changsha 410000, China
* Correspondence: taozhong@kust.edu.cn

Abstract: L-shaped concrete-filled steel tubular (CFST) columns, a kind of structural member appropriate for high-rise buildings, not only avoid the defect of conventional square columns protruding from the wall but also have the green and low-carbon properties of steel structures appropriate for fabricated construction. To learn more about their axial compression behavior, refined 3D finite element models were established using the general finite element software ABAQUS. The reliability of the models was subsequently verified based on failure tests and load–displacement relation tests on eight L-shaped specimens. The axial compression mechanism of L-shaped CFST columns was investigated using the verified finite element models. Further systematic parameter analysis was carried out to investigate the influence of parameters such as steel strength, concrete strength, length ratio of long limb to short limb, the angle between the two limbs, and combination methods on the axial compression behavior of L-shaped CFST columns. The results demonstrate that the angle between the two limbs has a significant impact on the stress distribution of concrete and steel pipes. The corner effect increases as the angle between the two limbs decreases. The combination of F-type specimens can better exert the constraint effect of steel pipes on concrete, while the triangular cavity of unequal-limb specimens and specimens with an included angle of 60° cannot effectively trigger the interaction between steel pipes and concrete. The initial stiffness of L-shaped CFST columns increases with an increase in concrete strength and a decrease in limb length ratio, which is not sensitive to changes in steel strength and the included angle. The peak bearing capacity of the specimens increases with increases in steel strength and concrete strength and a decrease in the limb length ratio. Compared to C-type and Z-type specimens, the initial stiffness of F-type specimens is slightly higher, and the peak bearing capacity is significantly increased.

Keywords: L-shaped concrete-filled steel tubular column; axial compression behavior; finite element analysis; combination method

check for updates

Citation: Li, H.; Tao, Z.; Han, D. Finite Element Analysis of Axial Compression Behavior of L-Shaped Concrete-Filled Steel Tubular Columns with Different Combinations. *Buildings* **2024**, *14*, 730. https://doi.org/10.3390/buildings14030730

Academic Editor: Rajai Zuheir Al-Rousan

Received: 24 January 2024
Revised: 21 February 2024
Accepted: 6 March 2024
Published: 8 March 2024

Copyright: © 2024 by the authors. Licensee MDPI, Basel, Switzerland. This article is an open access article distributed under the terms and conditions of the Creative Commons Attribution (CC BY) license (https://creativecommons.org/licenses/by/4.0/).

1. Introduction

The annual carbon emissions of the construction industry account for more than 40% of the total [1] when upstream and downstream businesses like transportation and the production of construction materials are taken into account. To achieve the objective of "carbon peaking and neutrality", it is crucial to promote the green transformation of the construction industry. When compared to concrete structures, steel structures are more ecologically friendly and have lower whole-life-cycle carbon emissions. W. Hawkins [2] compared the whole-life-cycle carbon emissions of concrete, steel, and timber structures and found that steel structures reduced carbon emissions by about 22% compared to concrete structures at all stages. Su [3] concluded that steel structures were more environmentally

friendly with less wet work than concrete structures, and a case study showed that steel structures emit 48.1% less carbon than concrete structures. After taking steel recycling into account, A. Zeitz's [4] study on four different structural forms of parking lots revealed that the carbon emissions of steel structures were only 38.3% of their original carbon content, a significantly lower percentage than for concrete structures. It is evident from the above study that steel structures fit the development needs of the green transformation in the construction sector since they are labor-saving, resource-conserving, and have a lower environmental impact during construction than traditional reinforced concrete structures cast in situ. Steel structures serve as crucial carriers for the advancement of a low-carbon economy and green environmental protection [5,6].

Due to the use of standard sections such as rectangular and H-shaped columns in traditional residential buildings with steel structures, the column ribs frequently protrude from the walls, which not only takes up limited indoor space but also impedes furniture deployment. Indoor appearance and functioning are negatively affected, posing a significant barrier to the development and application of prefabricated steel constructions in residential buildings. The advantages of high steel structure assembly level and great fire resistance of concrete structure are combined in the concrete-filled steel tubular structure, which has good economic benefits. For example, the interior convex angle achieved by utilizing square CFST columns can be handled by concealing the structural columns inside the wall with L-shaped or T-shaped CFST columns. CFST columns have been used in practical applications [7], as shown in Figure 1.



(**a**) CFST columns (**b**) Practical project

Figure 1. Engineering applications of CFST columns.

Numerous researchers have conducted research on the axial compression, eccentric compression, and seismic performance of L-shaped CFST columns. Zuo [8] conducted experiments on special-shaped columns with binding bars, and the results showed that the binding bars can effectively enhance the binding force of steel pipes on concrete. Zhou [9] investigated the effects of axial compression ratio and aspect ratio on the seismic performance of L-shaped CFST columns through experiments, studied the asymmetry character of the column, and carried out finite element analysis to simulate the behavior of SCFST columns. Shen [10] tested six specimens under constant axial and cyclically varying lateral loads to investigate the effects of width to depth ratio of section, depth to thickness ratio of steel tube, and axial load level on the strength, as well as stiffness, ductility, and energy dissipation of L-shaped CFST columns. Zheng [11] presented four tests carried out on multi-cell L-shaped CFST columns under combined constant compression and lateral cyclic loads. The main variables were loading angles and axial load levels. A finite element model was developed to simulate the multi-cell L-shaped CFST columns at different loading angles, and parametric analysis was conducted to evaluate the impact of various parameters on the lateral load–displacement curves of the columns under diagonal loading. Zhang [12] studied the seismic performance of nine L-shaped concrete-filled steel tubular columns and proposed the calculation formulas on the model curve based on the parameters, load, displacement, and stiffness degradation. Chen [13] proposed a prefabricated special-shaped concrete-filled steel tube with a rectangular multi-cell (S-CFST-R) column for residential systems, performed seismic testing of S-CFST-R columns, and verified the strong constraint effect of multi-cavity special-shaped CFST columns on concrete. Zhang [14] examined

the performance of a novel type of composite column: L-shaped columns comprising concrete-filled steel tubes joined by double-vertical steel plates (LCFST-D). Seven LCFST-D columns were tested under axial compression. Parametric experiments using the finite element model were conducted to investigate the effects of the thickness and width of the vertical steel plates. Wang [15] analyzed the axial behavior of an innovative L-shaped composite column. Seven specimens were evaluated to determine the failure progress, load capacity, and failure modes. The tested specimens exhibited shear failure with local buckling. Wang [16] tested eight SS-CFST columns to determine their axial compressive properties. Zhang [17] investigated the effects of eccentricity, column height, and sectional dimension on the stability performance of MCL-CFSTs columns.

Furthermore, some researchers have explored the constitutive relation and calculation formula of special-shaped CFST columns. Zhou [18] conducted experiments to investigate the biaxial loading behavior of L-shaped SCFT columns. Based on the findings, a reasonably simplified formula was proposed and proved effectively by comparing test results. Zheng [19] developed finite element models to simulate the axial behavior of unstiffened, stiffened, and multi-cell L-shaped and T-shaped CFST stub columns. A parametric study of 804 cases covering a wide range of parameters was conducted based on the FE models. New design models of axial compressive strength and stiffness were proposed. Lei et al. [20–22] proposed a uniaxial constitutive relation for T-shaped CFST columns based on fiber model analysis. Liu [23] experimented with six L-shaped and twelve T-shaped CFST stub columns under axial compression. Further parameter analysis with ABAQUS was carried out to study the influences of the steel ratio α, steel yield strength f_y, concrete strength f_{ck}, and slenderness ratio λ. Based on the experimental results and FE analysis, design formulas for calculating sectional bearing capacity and stability bearing capacity of special-shaped CFST columns were proposed. Liu [24] calculated the N–M correlation curves of the L-shaped CFST columns by using a full-section plasticity method and proposed formulas for calculating the eccentric compression ultimate bearing capacity of L-shaped CFST columns. Xiao [25] carried out experiments on 32 specimens, including 16 short columns and 16 medium–long columns, and provided formulas for estimating the ultimate bearing capacity of short and medium–long composite columns. Based on limit state theory, Zhang [26] established a calculation method for the sectional flexural capacity of the W-LCFST column. Additionally, they analyzed the accuracy of predicting the compression and bending capacity of the W-LCFST column under positive and negative loads using Standard CECS159–2004, with the recommended correction value provided. Chen [27] designed formulas for the stable bearing capacity of SCFST columns. Tu et al. [28,29] analyzed the influence of parameters such as concrete and steel strength on L-shaped CFST columns through FEA and proposed a formula for calculating the axial compressive bearing capacity. Huang [30] proposed a design formula for the bearing capacity of ribbed L-shaped CFST columns that took into account improvements in concrete performance. Chen [31] proposed a simplified strength model of ECB for L-shaped CFST based on the composite yielding method. Zheng [32] proposed a practical design method for predicting the bearing capacity of L-shaped CFST columns.

In the current research, researchers typically use methods such as tied reinforcement, tension bars, welded stiffening ribs, and so on to postpone the local buckling of the steel pipe of the L-shaped CFST column and enhance the restraining effect of the steel pipe on the concrete. However, these methods are complicated in construction, inconvenient in construction, and have an impact on the appearance of the buildings. In addition, when carrying out building design, building designers usually need to consider lighting, ventilation, and other factors, resulting in the corners of the building plan not necessarily having right angles. However, most of the L-shaped CFST columns studied so far are equal-limb cross-sections with right angles, and research on L-shaped CFST columns with special angles (non-right angles) existing in engineering practice has not been reported.

Based on this, we proposed three combination forms of L-shaped CFST columns with cross-section combinations. These forms are simple to assemble and do not alter

the building's appearance. The cross-sectional form is shown in Figure 2, where the F-type specimen is composed of square steel pipes, the C-type specimen is composed of square steel pipes and C-shaped cold-formed components, and the Z-type specimen is composed of C-shaped and Z-shaped cold-formed components. Experiments to investigate the mechanical behavior of the three combination forms of L-shaped CFST columns were conducted by our research team.

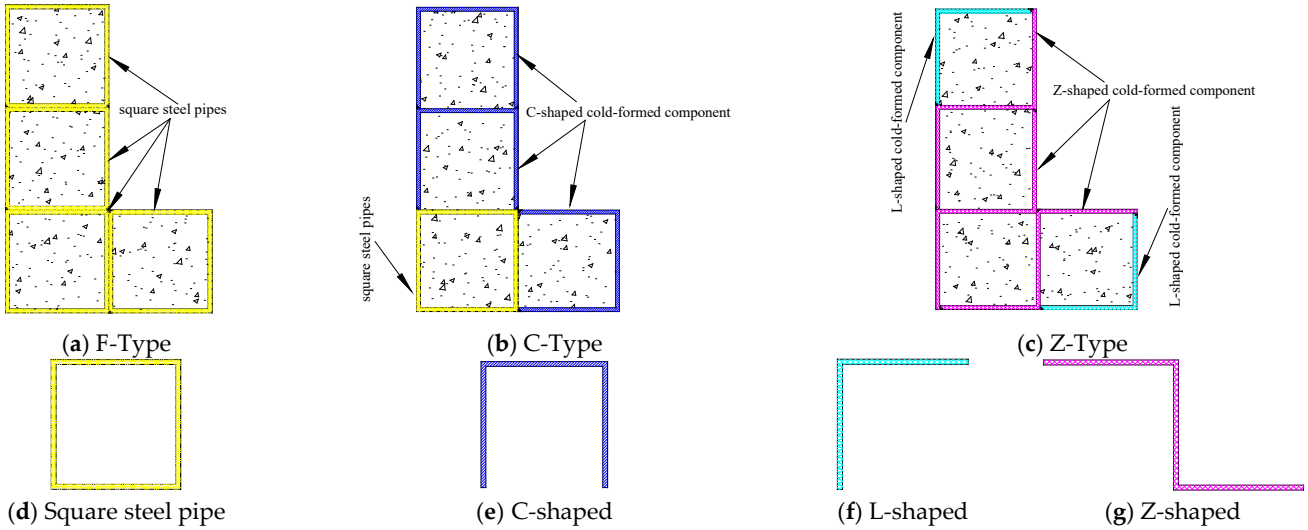


Figure 2. Types and components of L-shaped CFST columns.

This study proposed a refined numerical model of the specimens using ABAQUS to further investigate the axial compression mechanism of L-shaped CFST columns. The reliability of the model was verified using the obtained test results, and the impact patterns of different parameters were studied through extensive parameter analysis to clarify the interaction mechanism between steel pipes and concrete in L-shaped CFST.

2. Test Profile

Eight specimens were designed and manufactured to investigate the effects of combination methods, the length ratio of long limb to short limb, and the angle between the two limbs on the axial compression behavior of L-shaped CFST columns. The major parameters and test results of the specimens are listed in Table 1. To investigate the axial bearing capacity of L-shaped CFST columns, a 1000 kN compression testing machine was employed, as shown in Figure 3. The axial displacement of the specimen was measured by the displacement capture device at the loading end. Vertical and transverse strain gauges were attached at the mid-section of each specimen.

Table 1. Major parameters and results of test specimens.

Specimen No.	t/mm	H/mm	Concrete Grade	Steel Grade	d_u/mm	N_u/KN
AF-1.5-90°	3.75	600	C35	Q235	11.72	2685.8
AFD-1-90°	3.75	600	C35	Q235	10.12	3224.8
AC-1.5-90°	3.75	600	C35	Q235	7.46	2311.9
ACD-1-90°	3.75	600	C35	Q235	10.55	2975.0
AZ-1.5-90°	3.75	600	C35	Q235	7.97	2229.5
AZD-1-90°	3.75	600	C35	Q235	8.54	2945.8
ACD-1-60°	3.75	1200	C35	Q235	11.15	2315.2
ACD-1-135°	3.75	1200	C35	Q235	16.61	3352.9

Where A represents the axially loaded specimen; F, C, and Z refer to the type of specimen; D indicates an equal length of the two limbs; 1.5 and 1 represent the length ratio of the long limb to short limb; 90°, 60°, and 135° represent the angle between the two limbs; t is the thickness of the steel; H is the height of the column; d_u represents the peak displacement of the specimen; N_u represents the peak bearing capacity of the specimen.



Figure 3. Typical loading diagram.

Using a graded loading approach, the test was run for two minutes, with each stress level representing about one-tenth of the anticipated axial compressive load capacity. Once the specimen reached its yield strength, the load range was whittled down to one-fifteenth of its axial compressive load capacity. Loading proceeded gradually as the anticipated ultimate load approached, and it ceased when the load capacity decreased to 60% of the ultimate load capacity or there was noticeable deformation.

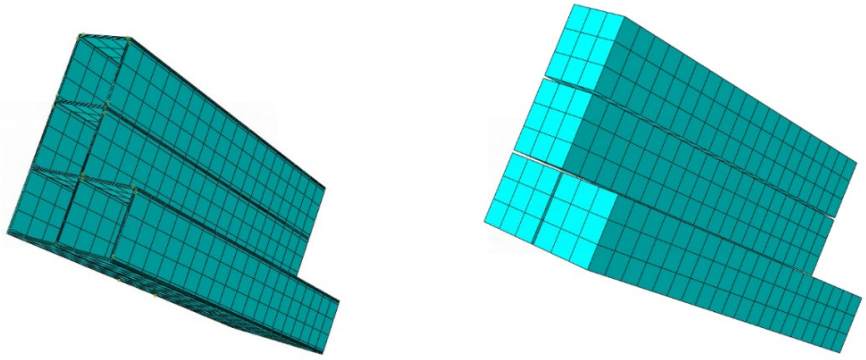
3. Finite Element Model (FEM)

Finite element analysis (FEA) has become an invaluable part of most structural studies since it can be used as an efficient tool to investigate structural behaviors, especially the composite actions between components of CFST specimens. Numerous researchers have investigated the mechanical performance of L-shaped CFST columns through ABAQUS. Zheng [11] investigated the effects of various parameters on lateral load–displacement curves of L-shaped CFST columns under diagonal loading. Chen [13] analyzed the influence of different loading directions on the ultimate bearing capacity of L-shaped CFST columns. Wang [15] conducted parametric analysis to investigate the influence on the axial behavior of L-shaped CFST columns. Liu [23] analyzed the axial compression behavior of L-shaped CFST columns through ABAQUS.

According to the aforementioned research, ABAQUS was able to accurately model the mechanical behavior of L-shaped CFST columns. In this paper, refined numerical models of the specimens were proposed using ABAQUS to further investigate the axial compression mechanism of L-shaped CFST columns.

3.1. Model Unit Selection and Meshing

The same model was employed for C-type and Z-type specimens due to their similar ultimate bearing capacities and failure modes. ABAQUS models were established for all specimens. Each component of the FEM adopts a 3D solid (C3D8R) in a reduced integral format and is meshed based on the following principles: (1) the number of grid layers in the thickness direction of steel pipe components shall not be less than 2; (2) to achieve reliable modeling with minimum increase in computational consumption, mesh convergence studies were conducted to determine the appropriate mesh size; (3) the steel pipe serves as the master surface, with a mesh size of 30 mm; the concrete serves as the slave surface, with a mesh size of 28 mm. The components and meshing are displayed in Figure 4.



(**a**) Steel pipe (**b**) Concrete

Figure 4. Components and meshing.

3.2. Material Constitutive Relations

3.2.1. Steel Constitutive Relation

Based on the constitutive relation of steel proposed in the literature [33], this study simulated the elastic–plastic properties of steel used in axial compression tests. Figure 5 displays the uniaxial stress–strain relation curve of steel, with f_p, f_y, and f_u representing the proportional limit, yield strength, and tensile strength of the steel, respectively; ε_e is the strain corresponding to f_p; ε_{y1} and ε_{y2} represent the strain corresponding to the starting and ending points of the yield plateau; ε_u is the strain corresponding to f_u.

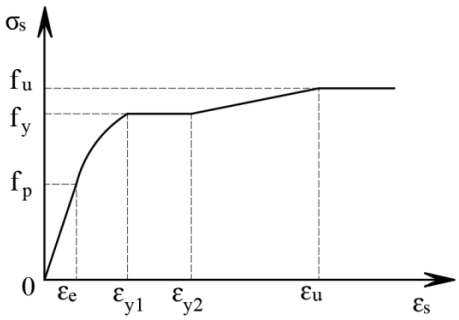


Figure 5. Stress–strain curve of Q235 steel.

The stress–strain relationship of steel is described as follows:

$$\sigma_s = \begin{cases} E_s\varepsilon_s & (\varepsilon_s < \varepsilon_e) \\ -A{\varepsilon_s}^2 + B\varepsilon_s + C & (\varepsilon_e < \varepsilon_s \le \varepsilon_{y1}) \\ f_y[1 + 0.6\frac{\varepsilon_s - \varepsilon_{y2}}{\varepsilon_{y3} - \varepsilon_u}] & (\varepsilon_{y2} < \varepsilon_s \le \varepsilon_u) \\ 1.6f_y & (\varepsilon_s \ge \varepsilon_u) \end{cases} \quad (1)$$

where the elastic modulus of steel $E_s = 2.06 \times 10^5$ MPa; Poisson's ratio is 0.3; $\varepsilon_e = 0.8\,f_y/E_s$; $\varepsilon_{y1} = 1.5\,\varepsilon_e$; $\varepsilon_{y2} = 10\,\varepsilon_{y1}$; $A = 0.2\,f_y/(\varepsilon_{y1} - \varepsilon_e)^2$; $B = 2\,A\varepsilon_{y1}$; $C = 0.8\,f_y + A{\varepsilon_e}^2 - B\varepsilon_e$.

3.2.2. Concrete Constitutive Relation

This study adopts the constitutive relation of concrete proposed in the literature [33,34] based on the research of CFST columns, as shown in Figure 6.

The compressive stress–strain relationship of concrete is described as follows:

$$y = \begin{cases} 2x - x^2 & (x \le 1) \\ \frac{x}{\beta_0(x-1)^\eta + x} & (x > 1) \end{cases} \quad (2)$$

where $x = \varepsilon/\varepsilon_0$; $y = \sigma/f_{c0}$; $f_{c0} = f_c\,[1 + (-0.0291\,\xi^2 + 0.1189\,\xi) \times (22.8/f_c)^{0.3048}]$; $\varepsilon_0 = [(1300 + 12.5\,f_{c0}) + 800\,\xi^{0.2}] \times 10^{-6}$; $\eta = 1.6 + 1.5/x$; $\beta_0 = (f_c)^{0.1}/1.2\,\sqrt{1+\xi}$. $\xi = A_s f_y/A_c f_{ck}$. ε is the

compressive strain of concrete; ε_0 is the peak compressive strain of concrete considering the constraint effect; σ is the compressive stress of concrete; f_{c0} is the peak compressive stress of concrete after considering the constraint effect; f_c is the compressive strength of the concrete prism; f_{ck} is the standard value of axial compressive strength of concrete; A_s and A_c represent the areas of steel and concrete, respectively; ξ is the equivalent coefficient of constraint effect; and η and β_0 are coefficients.

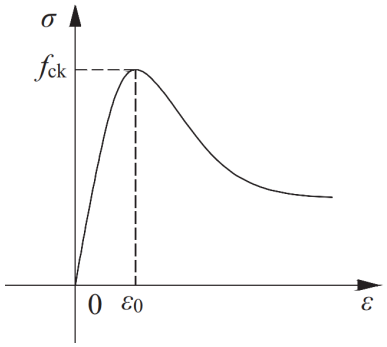


Figure 6. Stress–strain curve of concrete.

The concrete damage plasticity (CDP) module available in the material library of ABAQUS was used to describe the plastic behavior of the concrete infill in the FE model. For the inputs of the CDP module, constant values of 30, 0.1, 1.16, 2/3, and 0.0 were used for dilation angle (ψ), flow potential eccentricity (e), ratio of the compressive cylinder strength under biaxial loading to uniaxial compressive strength ($f_{b0}/f_{c'}$), and viscosity, respectively.

3.3. Model Interactions and Boundary Conditions

Surface-to-surface contact was adopted between the outer steel pipe and the in-fill concrete. Steel pipes and concrete are defined as the master surface and the slave surface, respectively, allowing the master surface to invade the slave surface but not vice versa. When the concrete contacts the steel tube due to its transverse deformation under axial compression, the concrete will be partially confined by the steel tube. To ensure that the two surfaces can separate from each other after contact, the normal contact attribute adopts hard contact, and the tangential contact attribute adopts a "penalty" function, with the friction coefficient being 0.6. The boundary condition and loading criterion are modeled completely according to those in the experiment. The upper and lower end plates were omitted in this model, making the same side of the concrete and steel pipe coupled with the coupling point. All the degrees of freedom (DOF) at the bottom of the model were confined throughout the calculation, while the top was totally constrained with the exception of releasing the Z-direction DOF. Axial displacement was used at the free end. The boundary conditions of the finite element model are displayed in Figure 7.

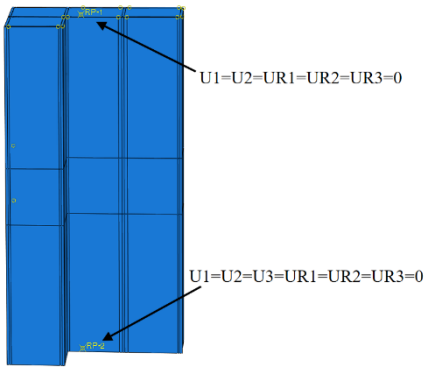


Figure 7. Boundary conditions of the finite element model.

4. Model Verification

4.1. Load–Displacement Curve Comparison

To verify the reliability of the FEM, the FEA results were compared with test results, as shown in Figure 8 and Table 2. It can be seen that the variation trend of the finite element calculation curve is basically consistent with the curve of the test results. In the elastic stage, the measured stiffness is slightly smaller than that obtained through the FEM. This is mainly due to a certain gap between the steel pipe and the concrete. Therefore, there is no cooperative bearing between the steel pipe and concrete in the early stage of loading. In the elastoplastic stage, there are slight differences between the test and FEM calculation curves, with a small difference in ultimate bearing capacity between the two. According to Table 2, the maximum deviation is 8.7%, and the standard deviation is 0.12.

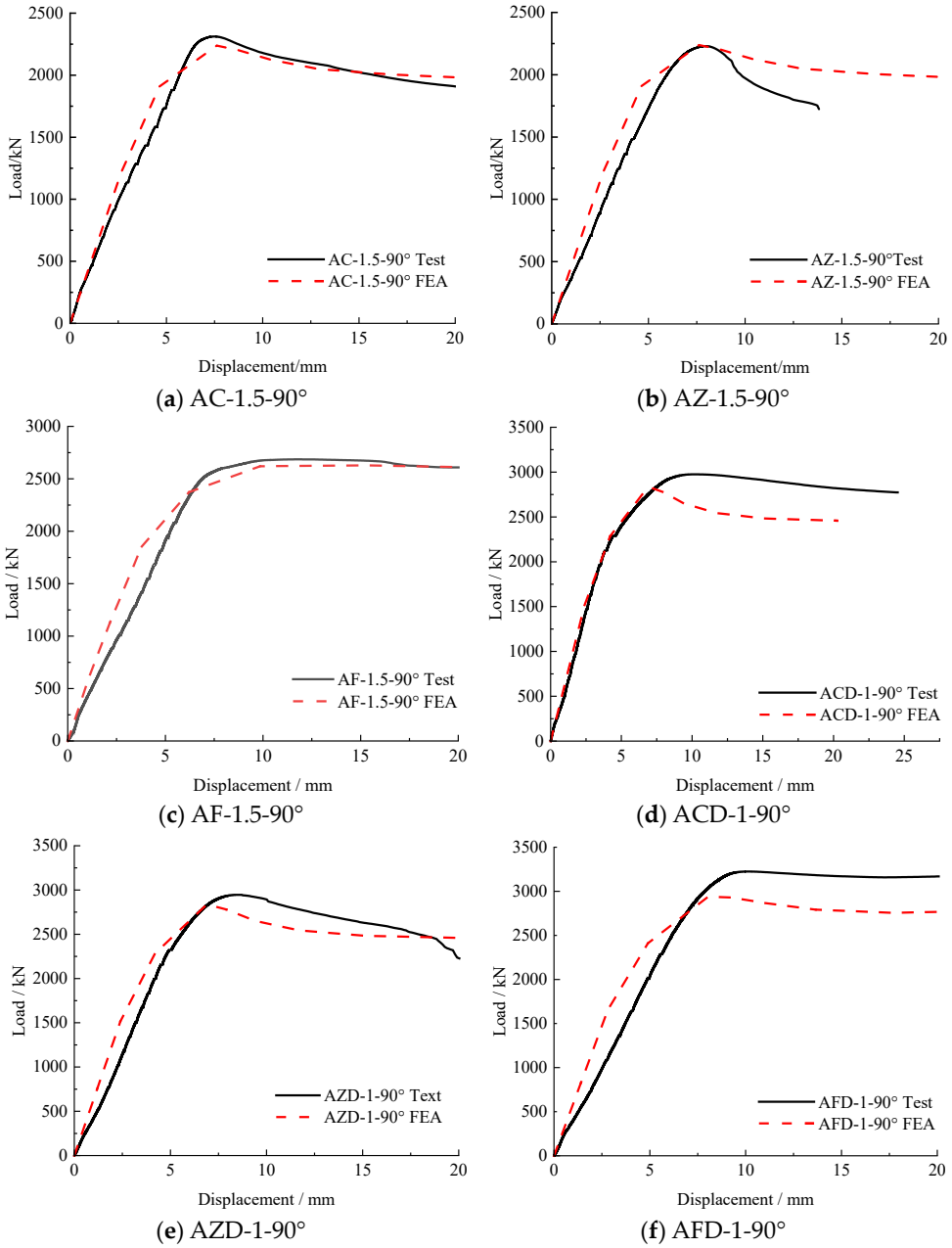
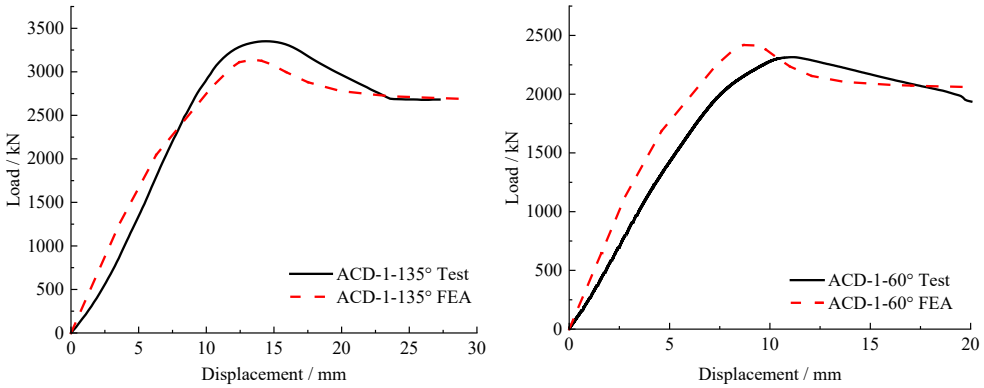


Figure 8. *Cont.*



(**g**) ACD-1-135° (**h**) ACD-1-60°

Figure 8. Load–displacement curve comparison.

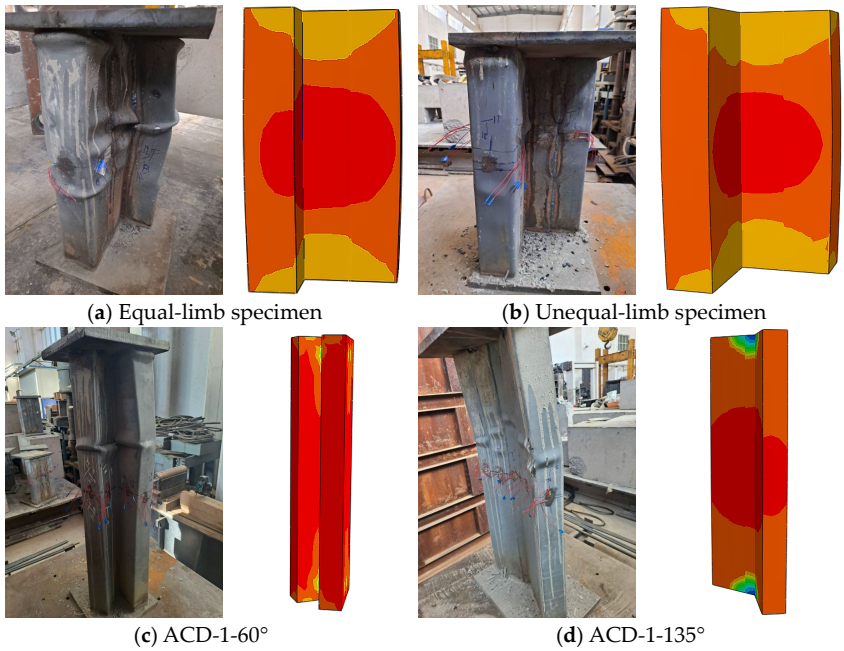
Table 2. Bearing capacity comparison.

Specimen No.	Specimen Size	K_{FE}	K_A	N_{FE}	N_A	N_{FE}/N_A	K_{FE}/K_A
AF-1.5-90°	300 × 200 × 100 × 600	490	374	2619.70	2679.30	1.023	1.309
AFD-1-90°	300 × 300 × 100 × 600	589	407	2938.96	3217.85	1.095	1.448
AC-1.5-90°	300 × 200 × 100 × 600	412	349	2238.21	2310.85	1.032	1.181
ACD-1-90°	300 × 300 × 100 × 600	632	582	2837.55	2969.25	1.046	1.086
AZ-1.5-90°	300 × 200 × 100 × 600	412	353	2238.21	2229.53	0.996	1.167
AZD-1-90°	300 × 300 × 100 × 600	632	459	2837.55	2940.52	1.036	1.377
ACD-1-60°	300 × 300 × 100 × 1200	367	290	2418.16	2314.62	0.957	1.262
ACD-1-135°	300 × 300 × 100 × 1200	325	287	3136.39	3352.61	1.069	1.133

Where K_{FE} represents the initial stiffness of the specimen in the FEA; K_A represents the initial stiffness of the test specimen; N_A represents the peak load of the test specimen; N_{FE} represents the peak load of the specimen in the FEA.

4.2. Failure Mode Comparison

Figure 9 compares the usual failure modes of the test specimens and the FEM. It is clear that the specimen bulges mostly at the ends and in the middle, not at the internal corners, which is typical in regular L-shaped CFST columns. This is due to the constraint effect of cavity walls on the internal corners in specimens. Overall, the FEM and material constitutive relation established in this study are reliable. Therefore, the proposed FEM can be a suitable tool for investigating the axial compression mechanism of L-shaped CFST columns.



(**a**) Equal-limb specimen (**b**) Unequal-limb specimen

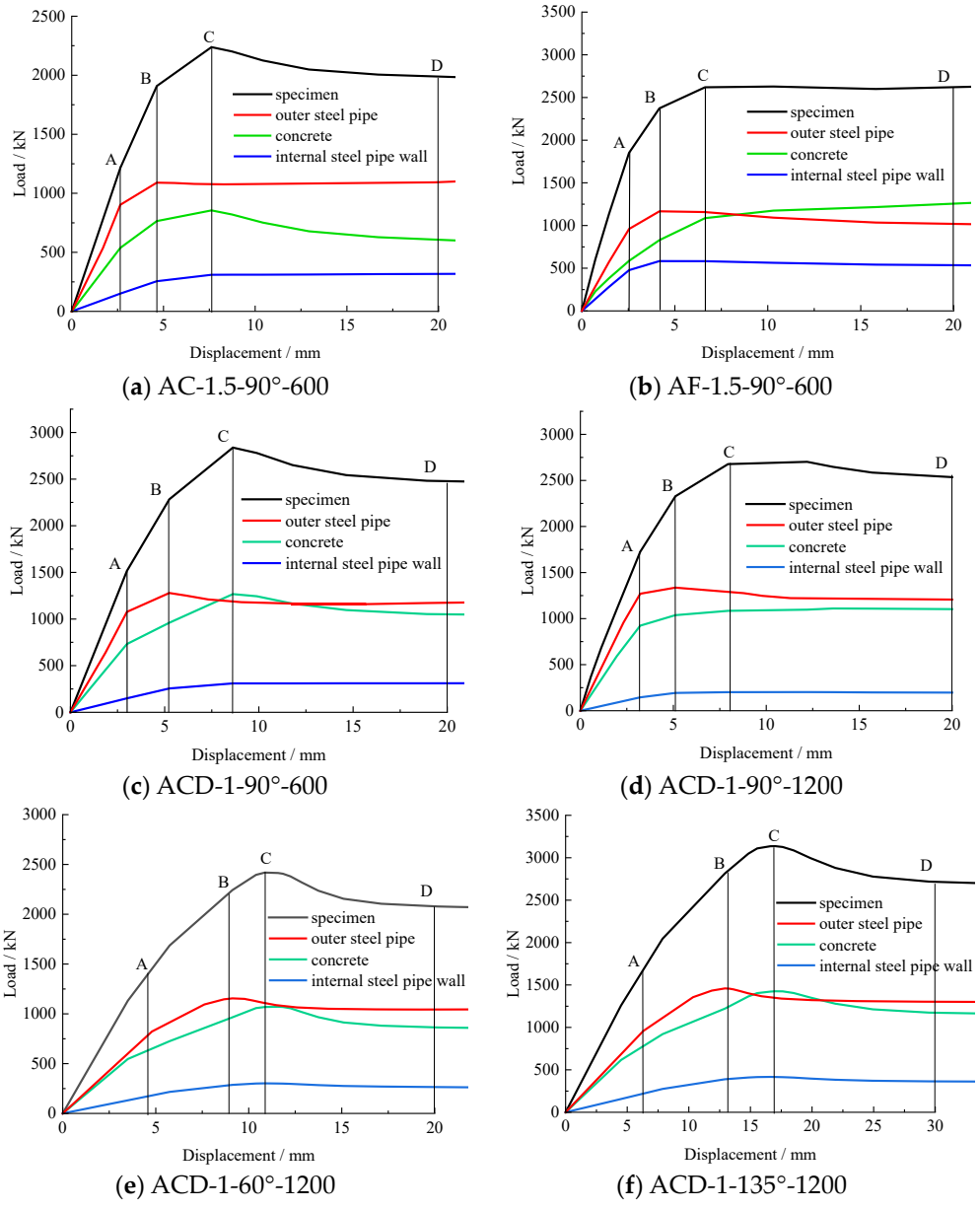
(**c**) ACD-1-60° (**d**) ACD-1-135°

Figure 9. Comparison of failure modes of test specimens and FEM.

5. Axial Compression Mechanism Analysis

5.1. Analysis of the Whole Stress Process of the Specimens

Based on the proposed FEM, axial compression analysis was conducted on L-shaped CFST columns. Figure 10 depicts the load–displacement curves of the specimens, including the load of concrete, outer steel pipes, and internal steel pipe walls. The load proportions of each part of the specimens are listed in Table 3. The loading procedure of all the specimens consists of four stages, with the four characteristic points marked on the curve. A depicts the elastic limit of the steel pipe. B indicates the point of buckling and local buckling of the steel pipe. C refers to the ultimate bearing capacity of the specimen. The displacement corresponding to point D is the failure displacement of the specimen.



(**a**) AC-1.5-90°-600 (**b**) AF-1.5-90°-600

(**c**) ACD-1-90°-600 (**d**) ACD-1-90°-1200

(**e**) ACD-1-60°-1200 (**f**) ACD-1-135°-1200

Figure 10. Load–displacement curves.

(1) O–A: The specimen is essentially in the elastic stage, where the load is increasing linearly and the steel pipes and concrete are each in a state of independent compression. The load–displacement curve of the steel pipe turns at point A, when the axial stress meets the yield stress of the steel pipe, and the slope of the specimen curve continues to decline.

(2) A–B: The specimen is in an elastic–plastic stage. Following point A, the load of the steel pipe still increases to a certain extent, and the load proportion of concrete continues to increase. The small cracks and lateral deformation inside the concrete gradually increase, and the stiffness of the specimen decreases to a certain extent.
(3) B–C: The specimen is in a plastic stage. Following point B, the overall bearing capacity of the specimen and the load of the concrete continue to increase. Moreover, due to the constraint effect of the steel pipe on the concrete, the bearing capacity of the concrete exceeds the compressive strength of the concrete block, while the load of the steel pipe begins to decrease to varying degrees. Compared to the other specimens, the 60° and 135° specimens exhibited more local buckling of the outer steel pipe, resulting in a more pronounced decrease in the load of the outer steel pipe. The outer steel pipes of the equal-limb specimen and the F-type specimen have a stronger constraint effect on the concrete than the unequal-limb specimen and the C-type specimen, resulting in a more significant rise in the load of the concrete of specimens ACD-1-90°-600 and AF-1.5-90°-600.
(4) C–D: The specimen is in the softening stage. Following point C, except Figure 10b,d, the overall bearing capacity of the rest of the specimens first shows a significant decrease and then tends to stabilize. The load of concrete gradually decreases due to intensified damage, while the load of the outer and inner steel pipe walls tends to stabilize.

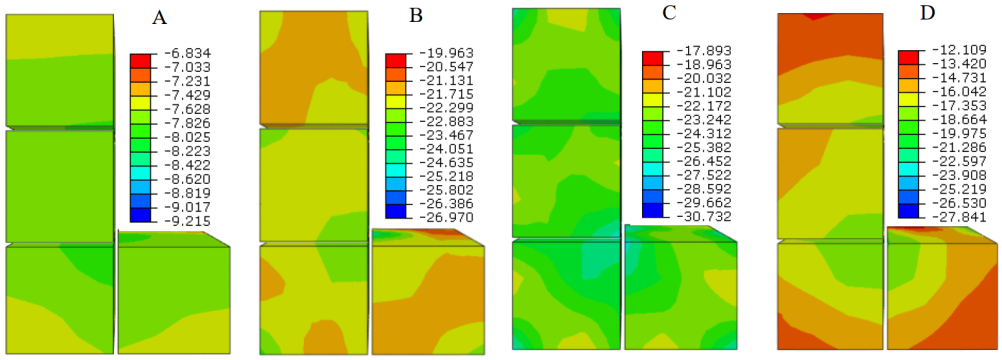
According to Figure 10b, following point C, the load of concrete does not appear to be significantly reduced, and the F-type specimen can be preferred in the actual project due to the stronger restraining effect of the steel pipe on the concrete in the F-type specimen and the difficulty of occurrence of unfavorable situations like weld decay during loading. According to Figure 10d, the reason for the apparent lack of significant reduction in the load of concrete could be attributed to the specimen's slight bending during the compression process after its height was increased. This led to a certain enhancement of the steel pipe's restraining effect on the concrete. Subsequent studies will delve into this phenomenon in further detail.

Table 3. Load proportions of each specimen part.

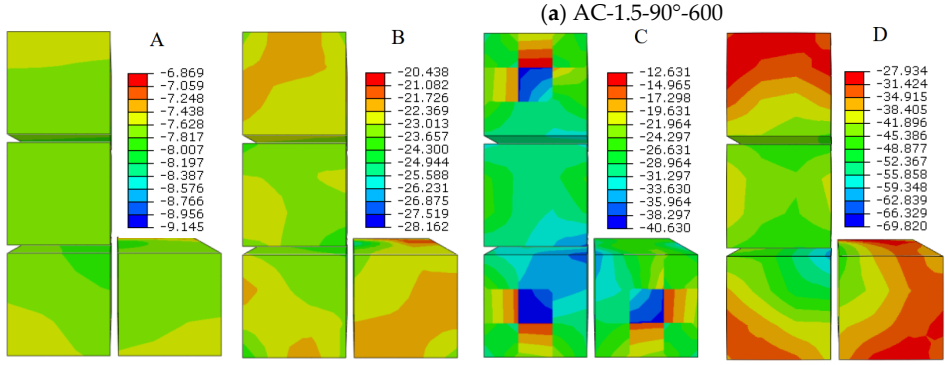
Specimen No.	H/mm	Outer Steel Pipe	Concrete	Internal Steel Pipe Wall
AC-1.5-90°-600	600	48.71%	38.20%	13.80%
AF-1.5-90°-600	600	44.29%	44.66%	22.32%
ACD-1-90°-600	600	45.08%	44.66%	10.89%
ACD-1-90°-1200	1200	49.86%	40.46%	7.54%
ACD-1-60°-1200	1200	47.27%	44.95%	12.41%
ACD-1-135°-1200	1200	46.52%	45.65%	13.23%

5.2. Stress Analysis of Concrete

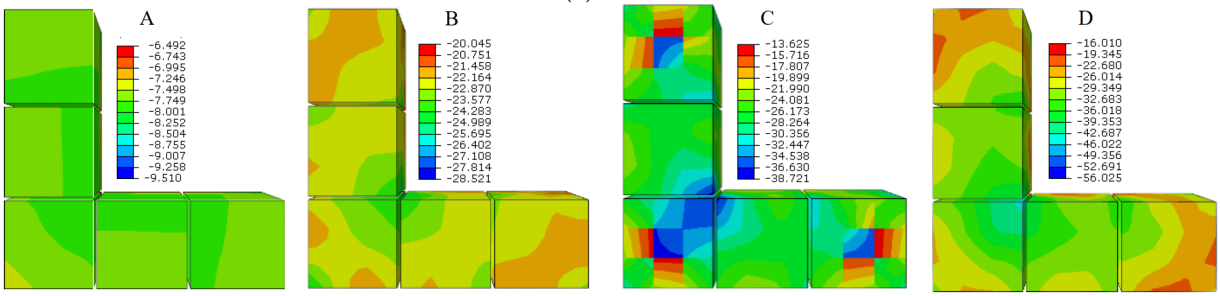
The stress states of each concrete specimen at four characteristic points are shown in Figure 11. From the beginning of loading to point A, the vertical stress distribution of the concrete in all the other specimens is relatively uniform except for specimen ACD-1-60°-1200, with a relatively large stress at its corner cavity, indicating that reducing the angle between the two limbs may easily lead to the corner stress concentration of the specimen in the initial loading stage. From A to B, the maximum vertical stress of the concrete gradually diffuses towards the outer edges and corners. Due to the corner effect, the stress in the specimen's corner cavity considerably rises when the included angle varies. When loaded to point B, the steel pipe reaches its maximum bearing capacity, while the concrete only reaches its maximum bearing capacity after point B. This is primarily due to the steel pipe's constraint effect on the concrete.



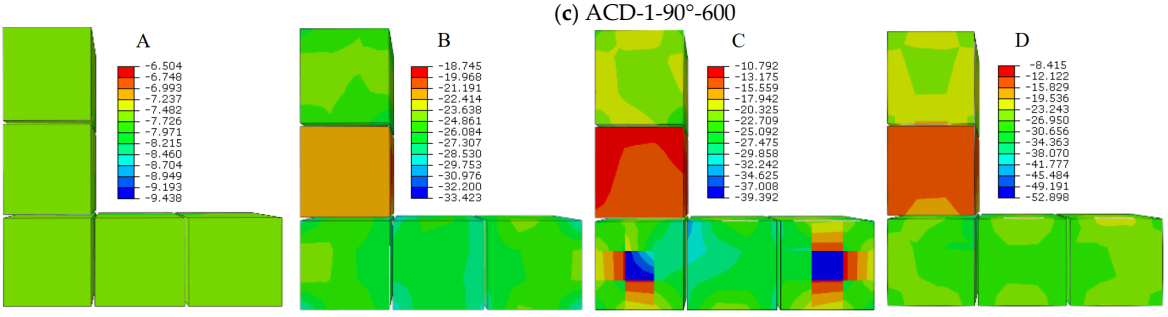
(**a**) AC-1.5-90°-600



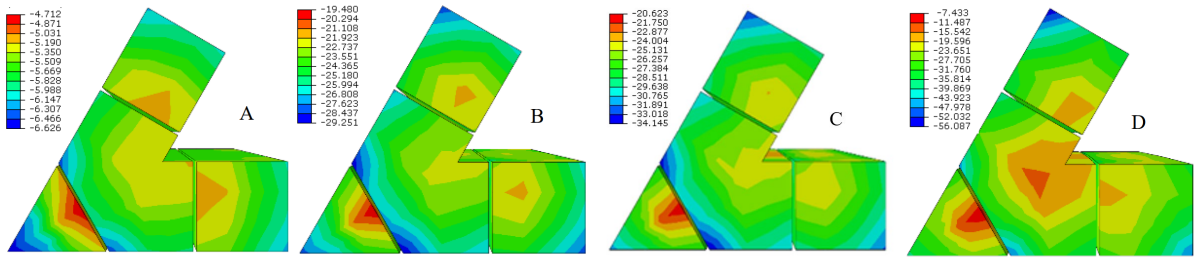
(**b**) AF-1.5-90°-600



(**c**) ACD-1-90°-600

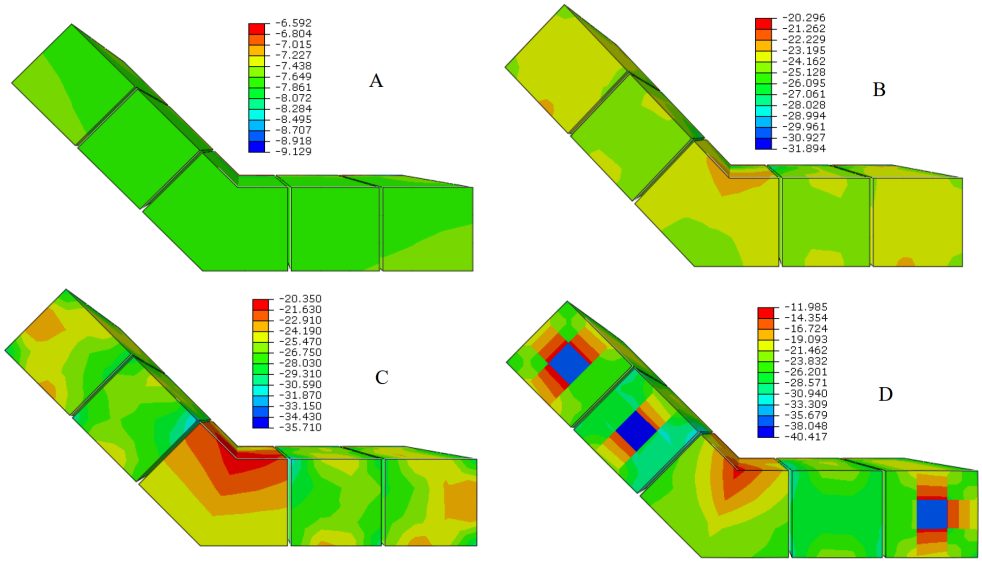


(**d**) ACD-1-90°-1200



(**e**) ACD-1-60°-1200

Figure 11. *Cont.*



(**f**) ACD-1-135°-1200

Figure 11. Stress nephogram of concrete.

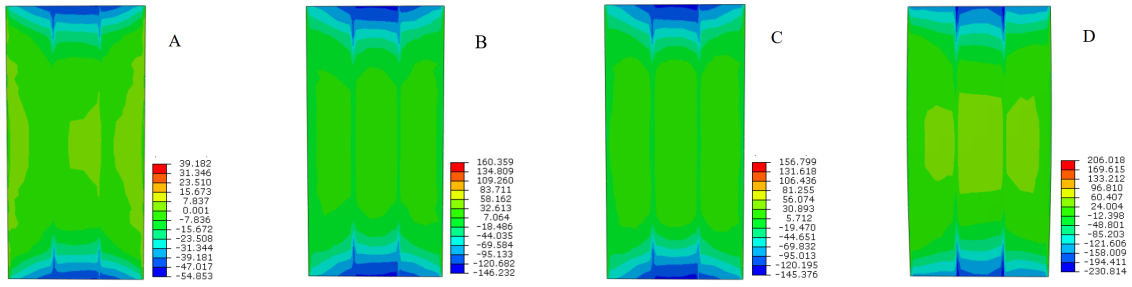
From B to C, the stress at the internal corner of the specimen with a 90° included angle rises from 24 MPa to 26 MPa, slightly higher than the stress at the external corner. As for the specimen with a 60° included angle, the stress at the internal corner increases from 21.92 MPa to 24.00 MPa, whereas the stress at the external corner increases from 29.25 MPa to 34.14 MPa. The greatest stress area at the external corner steadily diminishes, showing that decreasing the angle between the two limbs increases the corner effect of specimens. The stress at the internal corner of the 135° specimen drops from 22.22 MPa to 20.53 MPa, while the stress at the external corner remains unchanged. As can be observed, the angle between the two limbs has a major impact on the specimen's corner effect and stress distribution. From C to D, each specimen's high-stress zone appears at the 90° angle of the square cavity, with considerable fluctuations in stress at the internal and external corners. The stress in the corner cavity of some concrete specimens with the included angles of 60° and 135° diminishes because the stress area of the 135° and 60° corner cavities is smaller than that of the two flanges, with the other square cavities bearing the majority of the load. Therefore, in the actual engineering design for the special-angled L-shaped CFST columns, the angle between the two limbs should be considered in terms of the specimen's corner effect and stress distribution, and certain strengthening measures should be taken.

5.3. Stress Analysis of Steel Pipe

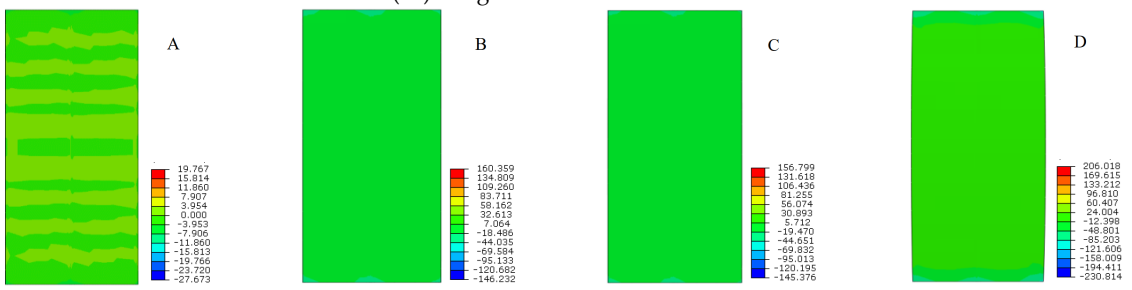
Figure 12 depicts the longitudinal stress nephogram of the steel pipe under the ultimate load for each specimen. Since there is little difference in the stress nephogram of the steel pipe between specimens AF-1.5-90° and AC-1.5-90°, specimen AC-1.5-90° was used as an example in this study. The figure shows that the steel pipe's stress distribution is symmetrical along the specimen's length from top to bottom. However, there are high-stress areas at the connection between the specimen and the upper and lower end plates, primarily because of the end plate's confinement effect on the steel pipe. Tensile stress appears in the middle of the specimen, mainly caused by local buckling of the steel pipe, and the maximum tensile stress zone is located in the middle of the specimen's cavity, indicating that the cavity can improve from single-wave buckling to multi-wave buckling.

As the limb length ratio increases, the long limbs of the unequal-limb specimen are characterized by multi-wave bulging, and the tensile stress in the middle of the cavity significantly increases. As the height increases, the tensile stress on the left flange of ACD-1-90°-1200 gradually concentrates in the middle of the two end cavities, while the tensile stress and distribution area in the middle cavity decrease, demonstrating that the two end cavities bear the majority of the load. As the included angle decreases, tensile stress gradually moves

towards the two cavities at the end of the left flange of ACD-1-60°-1200, with an increase to a certain extent, indicating that the cavity at the end of the flange serves as the primary load-bearing component of the specimen. As the included angle increases, the outer edge of the steel pipe of ACD-1-135°-1200 remains in a relatively uniform state in terms of tensile stress distribution. The tensile stress progressively increases with increasing load, owing primarily to the bending of the specimen, which is consistent with the test results.

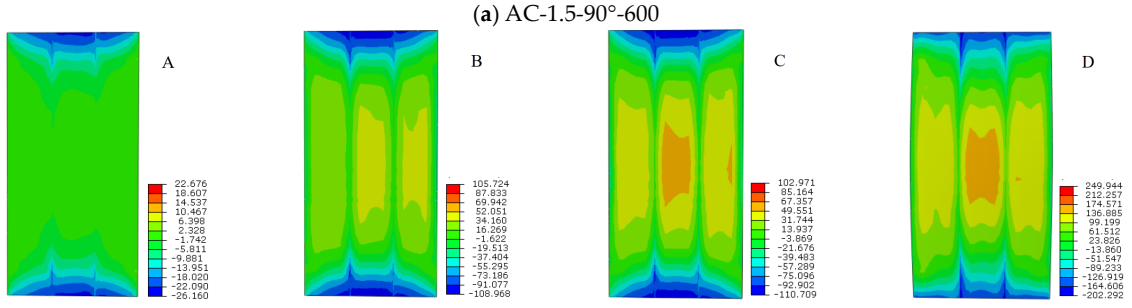


(**a1**) Long limb of AC-1.5-90°-600

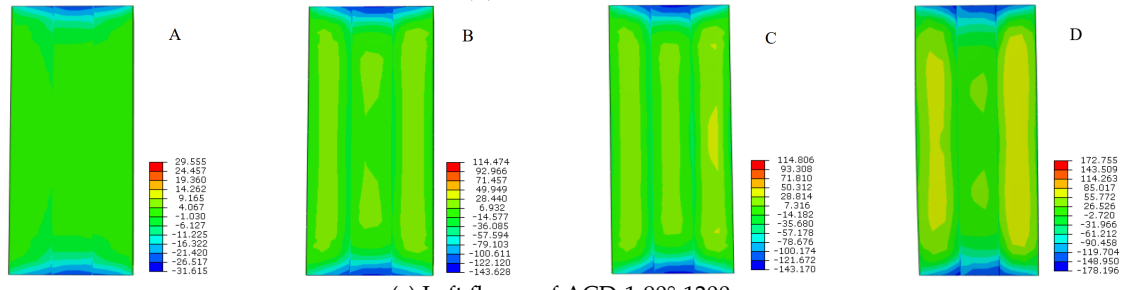


(**a2**) Short limb of AC-1.5-90°-600

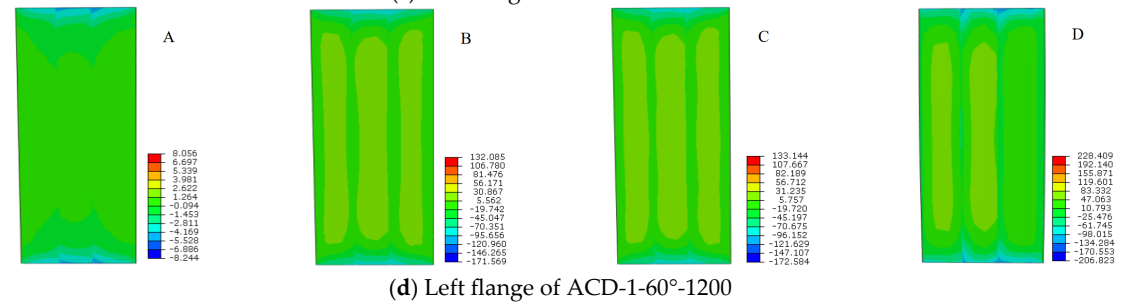
(**a**) AC-1.5-90°-600



(**b**) ACD-1-90°-600

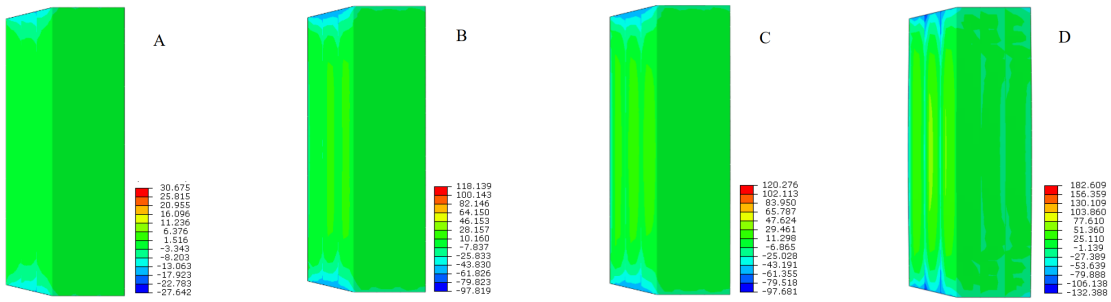


(**c**) Left flange of ACD-1-90°-1200



(**d**) Left flange of ACD-1-60°-1200

Figure 12. *Cont.*



(**e**) ACD-1-135°-1200

Figure 12. Stress nephogram of the steel pipes of specimens.

5.4. Interaction between Steel Pipes and Concrete

To further analyze the effects of the length ratio of long limb to short limb, column height, and the angle between the two limbs on the interaction between steel pipes and concrete, a curve was drawn to describe the magnitude and distribution of constraint stress by taking P_i and Δ as the horizontal and vertical coordinates. P_i is the contact stress, which can directly reflect the constraint effect; Δ represents the displacement. To avoid the corner effect of the steel pipe, the value of Pi was obtained from the middle of the specimen. The location of the contact stress point is shown in Figure 13. Figure 14 illustrates the P_i–Δ curves of the specimens.

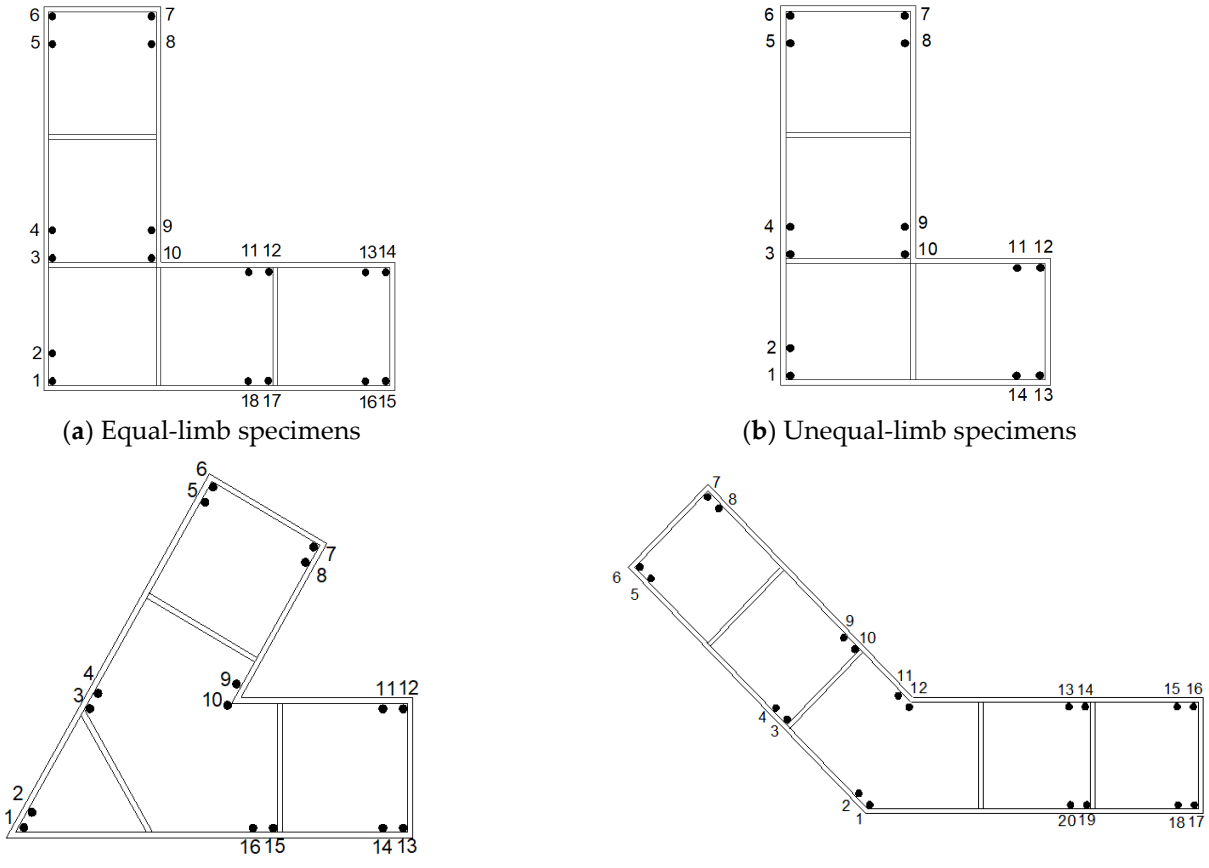
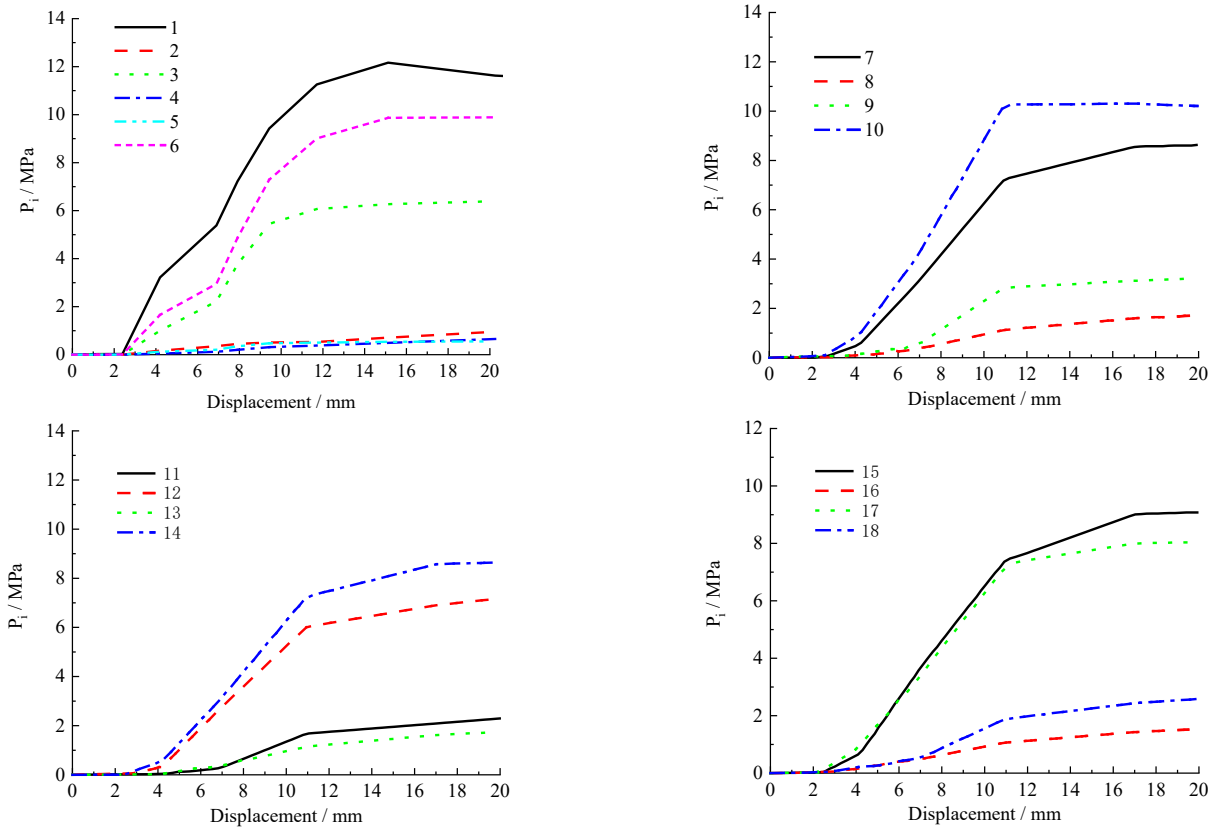
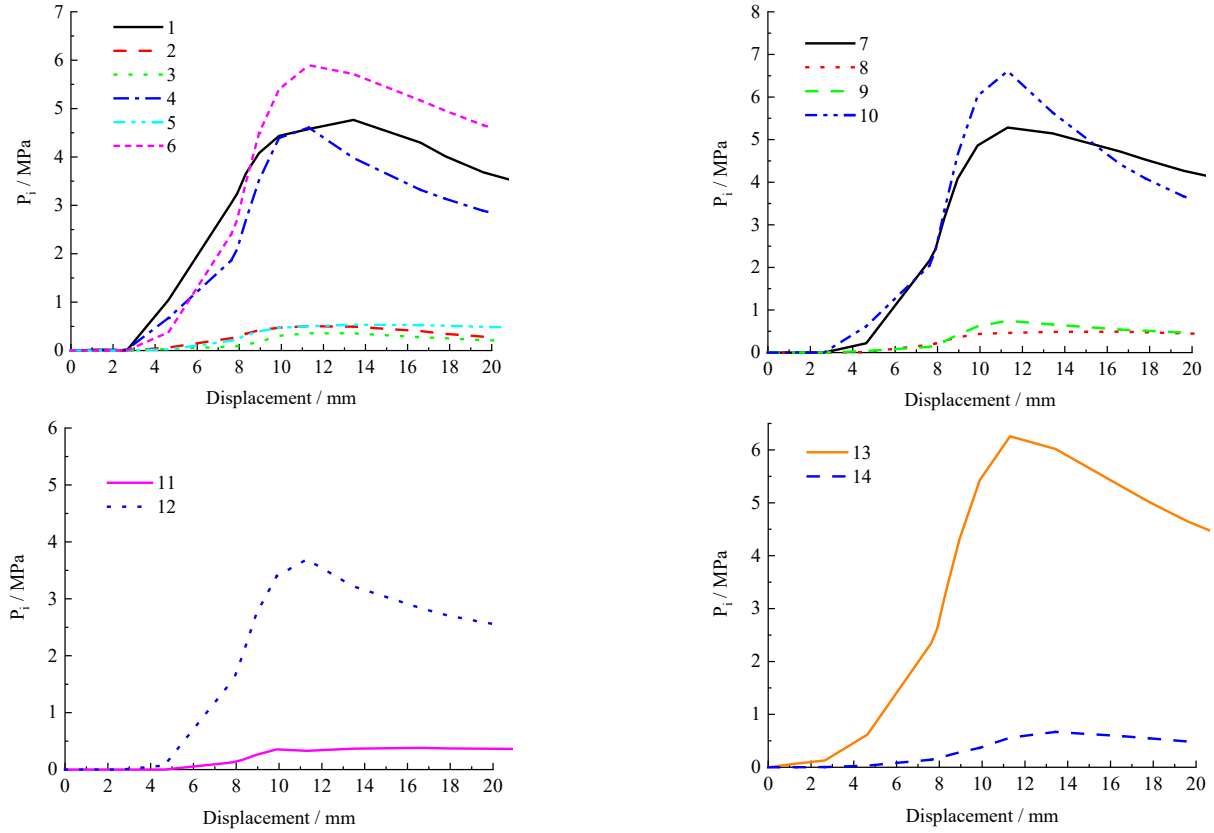


Figure 13. Locations of the contact stress points.

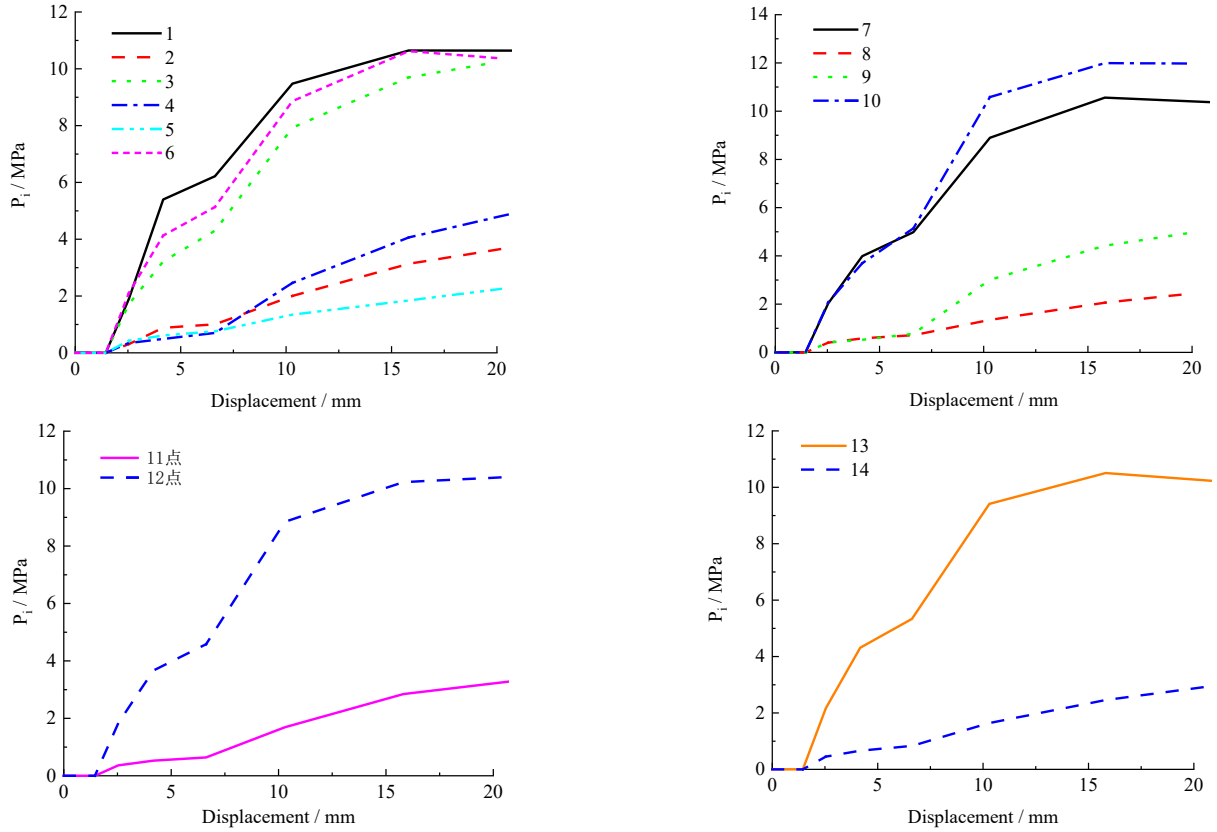


(**a**) ACD-1-90°-600

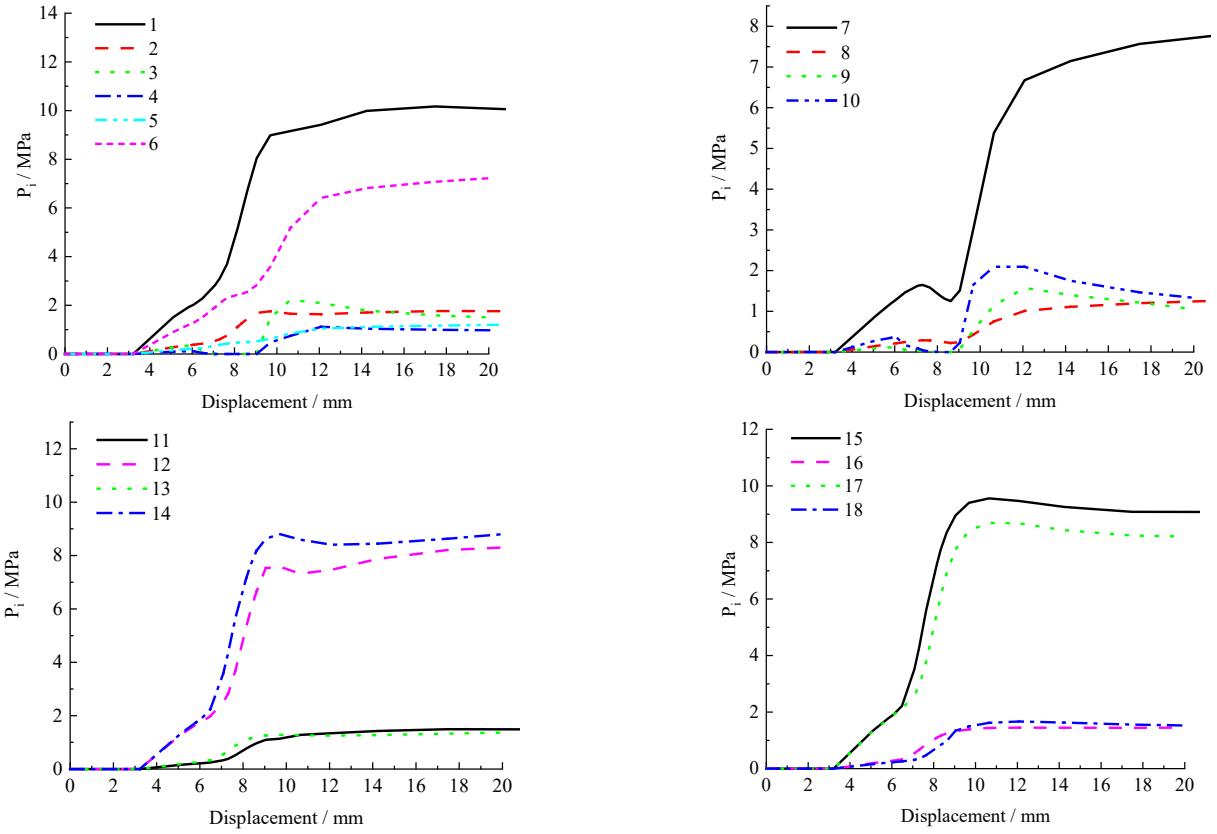


(**b**) AC-1.5-90°-600

Figure 14. *Cont.*

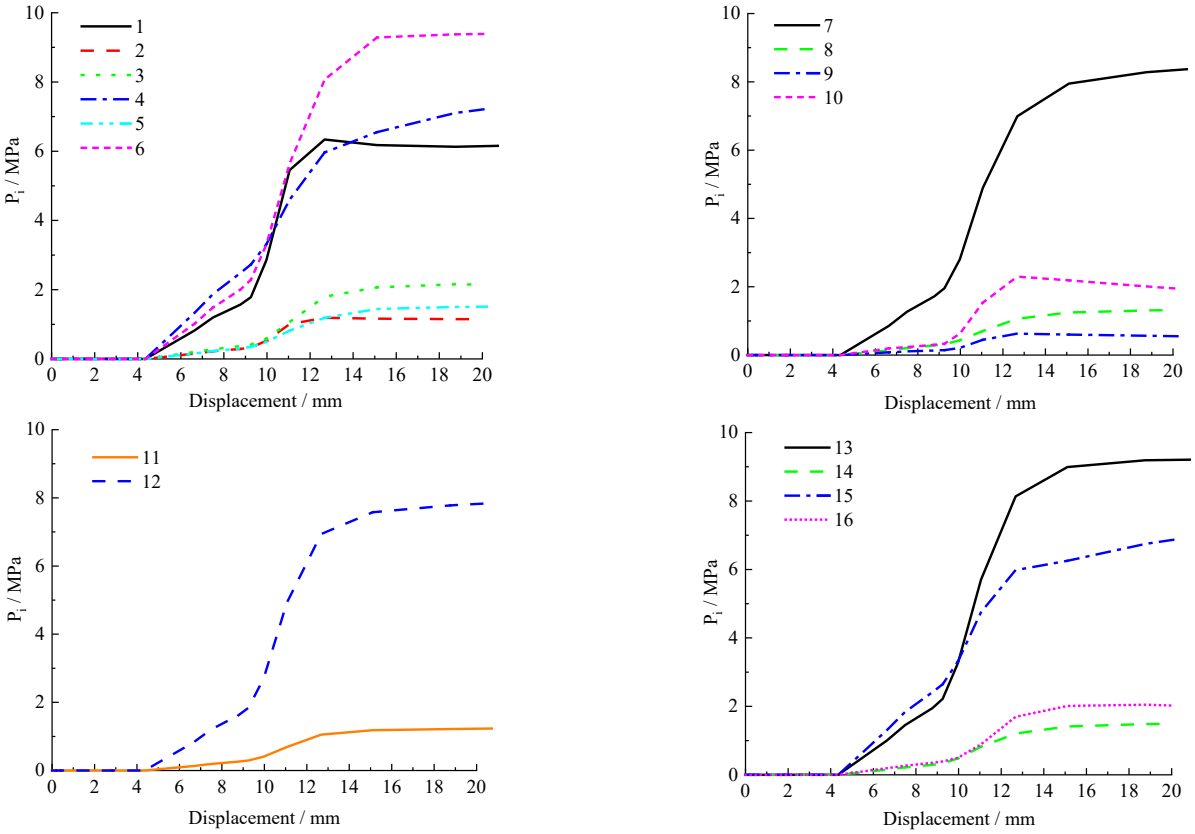


(**c**) AF-1.5-90°-600

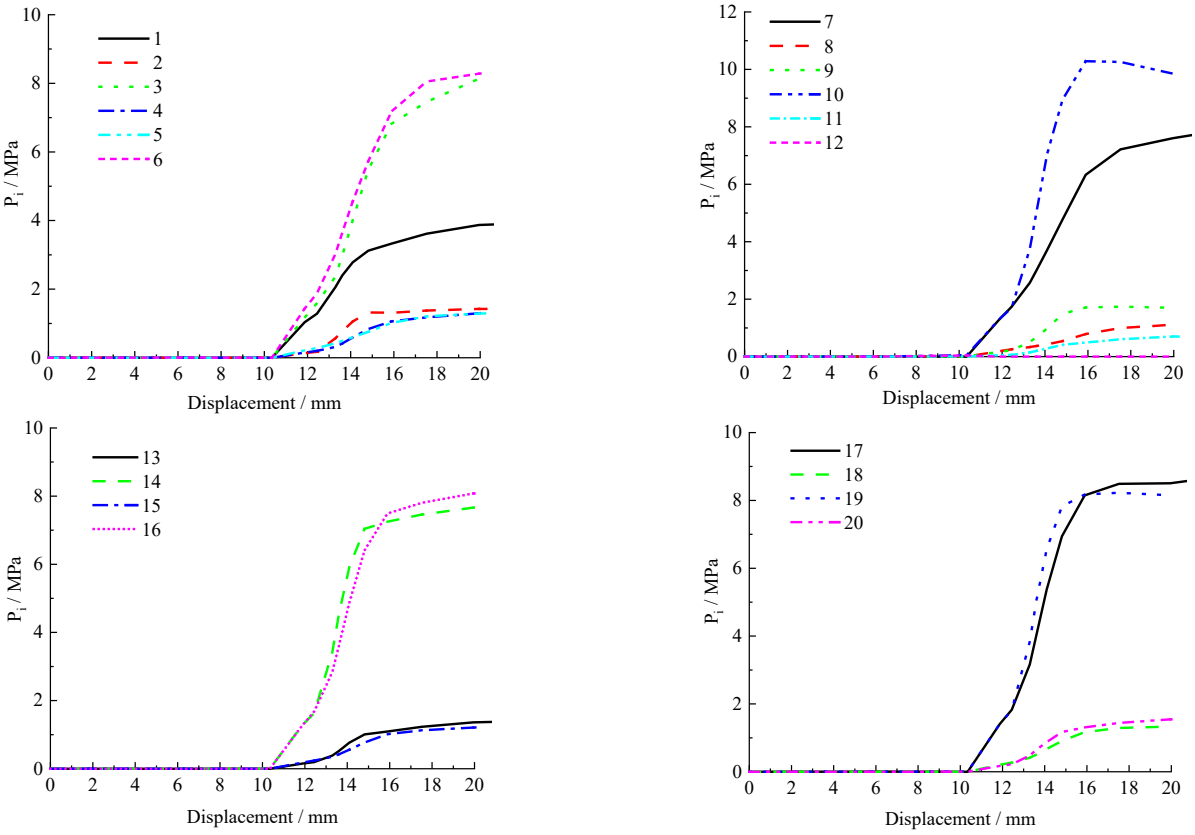


(**d**) ACD-1-90°-1200

Figure 14. *Cont.*



(**e**) ACD-1-60°-1200



(**f**) ACD-1-135°-1200

Figure 14. P_i–Δ curves of the specimens.

According to Figure 14, there was no contact stress between the steel pipe and the concrete during the initial loading stage. The high Poisson ratio of steel pipes resulted in more lateral deformation when compared to concrete. Small fractures arose in the concrete when the axial displacement increased, and the lateral deformation of the concrete exceeded that of the steel pipe, at which point contact stress occurred.

When compared to specimen ACD-1-90°-600, the contact stress of AC-1.5-90°-600 significantly declines after reaching its peak, as does the peak contact stress of corner points (such as points 1, 6, 7, and so on). At the later loading stage, the stiffness and bearing capacity fall faster. Furthermore, unlike in the case of equal-limb specimens, contact stress near the corners did not increase further in the later stage of loading. The circumstance described above shows that unequal-limb specimens cannot successfully exert an interaction between steel pipes and concrete.

The contact stress at and near the corners of specimen AF-1.5-90°-600 is significantly higher than that of AC-1.5-90°-600, and even slightly higher than that of ACD-1-90°-600, indicating that the square steel tube combination can better exert the contact effect between steel pipes and concrete. The corner contact stress of ACD-1-90°-1200 shows a similar development trend to that of ACD-1-90°-600, with the exception of a little drop in the later stage of loading, demonstrating that column height has a minimal effect on the interaction between steel pipes and concrete.

When the angle between the two limbs decreases to 60°, the peak contact stress at the external corner point (point 1) decreases, while the contact stress at the internal corner point (point 10) is at a lower level, indicating that the triangular cavity has a weaker constraint effect on the concrete. When the angle is increased to 135°, the occurrence time of contact stress at each point is much later than that of other specimens, indicating that the concrete failure of the specimens is relatively slow. In addition, the contact stress of each cavity on the two flanges of the specimen is not significantly different, indicating that the internal forces of each cavity in the specimen are relatively uniform.

6. Parametric Analysis

It has been shown that steel strength and concrete strength have an effect on the mechanical properties of L-shaped CFST columns, including initial stiffness, load capacity, and ductility [8,11,14,23]. In addition, the results of Wang [15] showed that the limb length ratio has an effect on the stiffness and load capacity of L-shaped CFST columns under axial pressure. Wang [35] found that the mechanical properties of specially angled columns differ from those of right-angled columns.

This study conducted parameter analysis based on the FEM proposed above to examine the influence of different parameters on the axial compression behavior of L-shaped CFST columns. The parameters include steel strength, concrete strength, length ratio of long limb to short limb, the angle between the two limbs, and the combination method.

6.1. Steel Strength

Figure 15 depicts the load–displacement curves of L-shaped CFST columns composed of different steel strengths. There is no significant difference in the initial stiffness of the columns, and the peak bearing capacity increases as the steel strength increases, which is consistent with Wang's findings [15]. Therefore, increasing the strength of steel does not effectively control the elastic displacement of L-shaped CFST columns in practical engineering design.

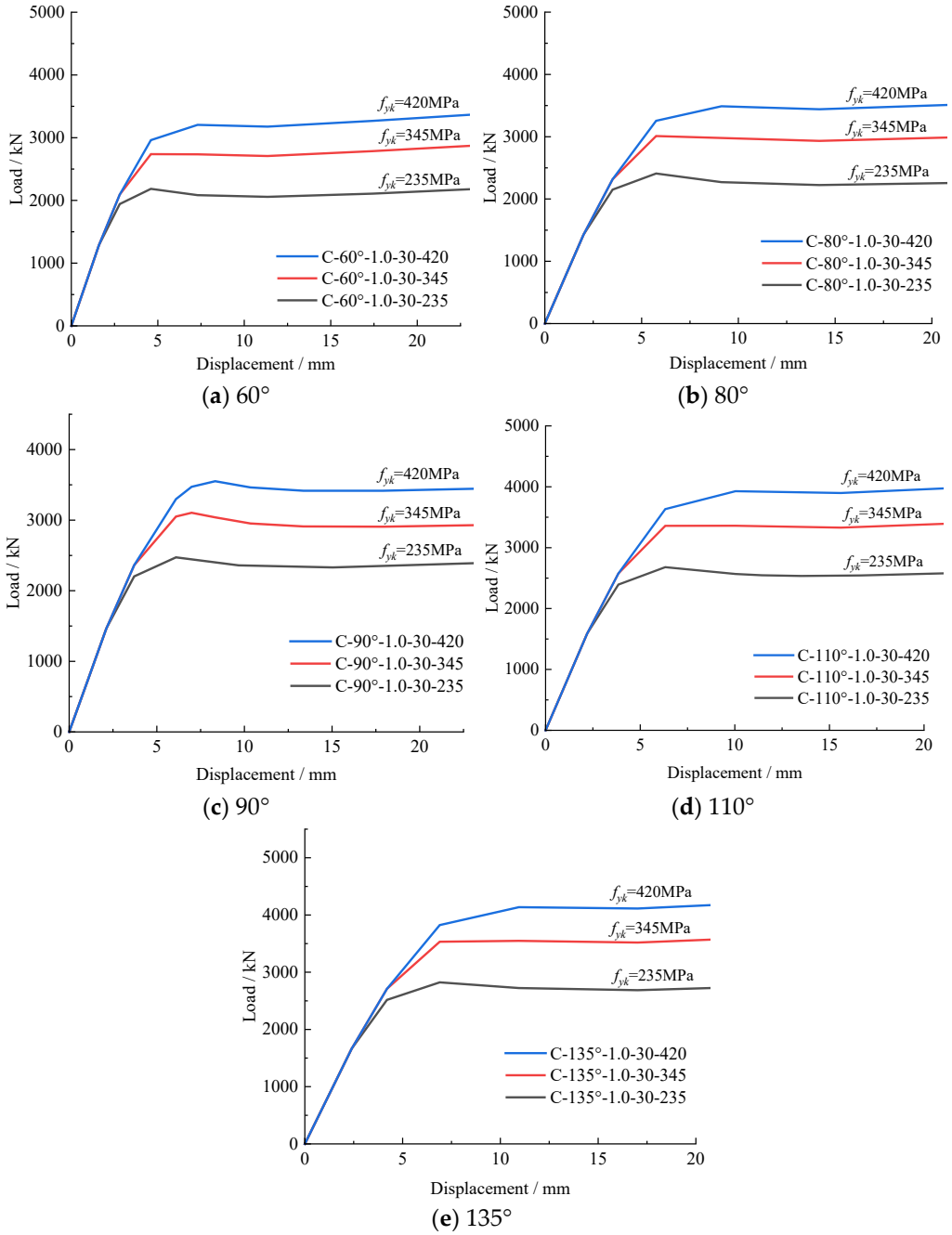


Figure 15. Load–displacement curves of specimens with different steel strength. Note: taking specimen C-60°-1.0-30-235 as an example, C represents the type of specimen; 60° represents the angle between the two limbs; 1.0 represents the length ratio of long limb to short limb; 30 represents the concrete strength; 235 represents the steel strength.

6.2. Concrete Strength

In the case of different angles between the two limbs, changing the concrete strength while keeping the other parameters unchanged, the load–displacement curves of each specimen can be obtained as shown in Figure 16. It can be seen that increasing concrete strength can significantly improve the initial stiffness of the specimen, and the peak bearing capacity of the specimen increases as the concrete strength increases, which is consistent with the conclusions in the literature [15]. In addition, the degree of reduction in the peak bearing capacity of the specimens increases with the increase in concrete strength. Therefore, this phenomenon should be noted if high-strength concrete is used in practical applications.

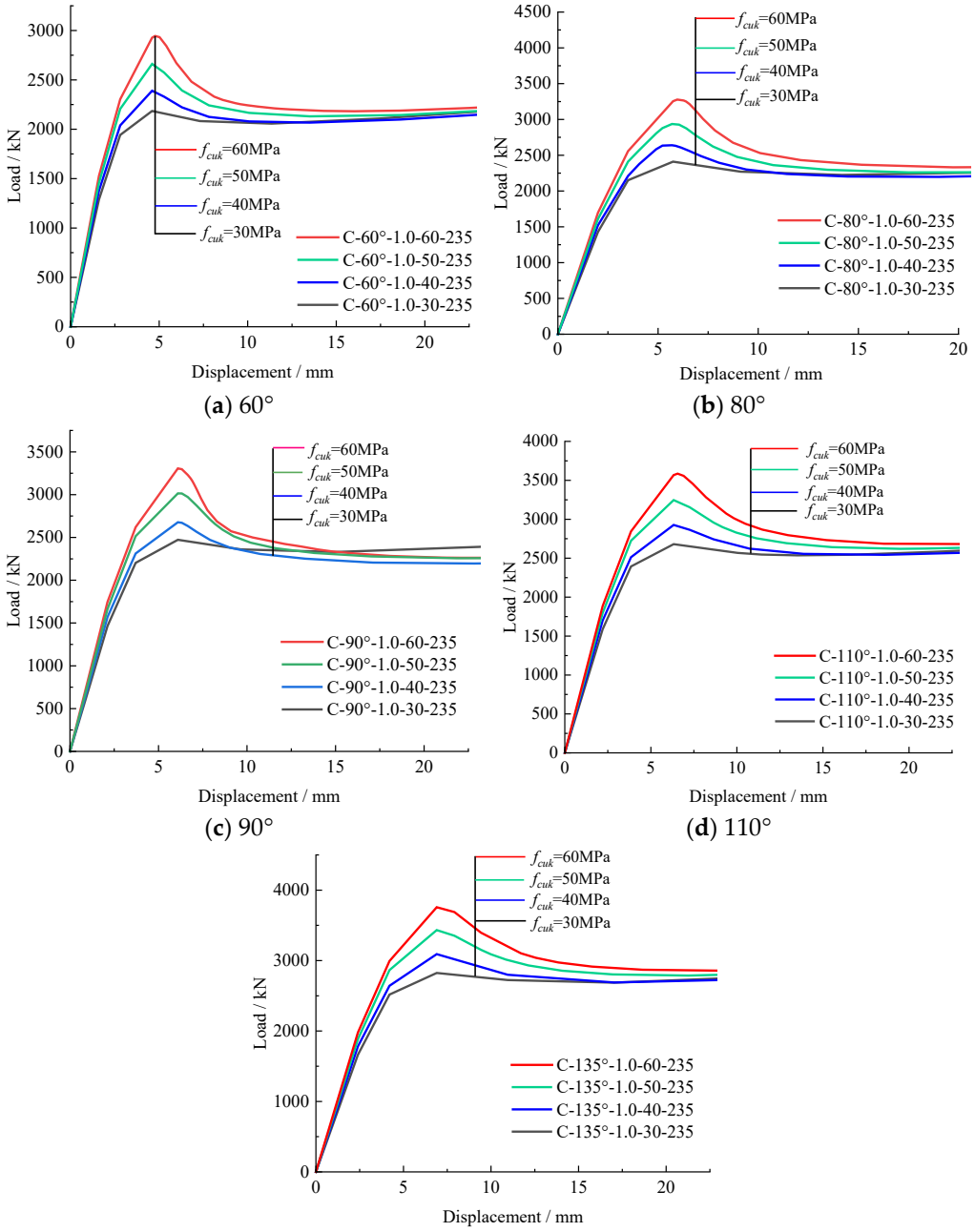


Figure 16. Load–displacement curves of specimens with different concrete strength.

6.3. Length Ratio of Long Limb to Short Limb

Figure 17 depicts the load–displacement curves of specimens with different angles between the two limbs and limb length ratios of 1.0, 1.2, 1.5, 1.7, and 2.0. It can be seen that, as the limb length ratio increases, the initial stiffness and the peak bearing capacity of the specimen both decrease. When the limb length ratio reaches 1.5, the loss in peak bearing capacity increases abruptly due to the reduction in one cavity in the short limb. Notably, there was no significant change in the peak displacement of specimens with different limb length ratios. Based on the aforementioned results, it can be concluded that an increase in limb length ratio has a significant impact on the initial stiffness and peak bearing capacity of L-shaped CFST columns, which is in line with the findings in the literature [15]. To guarantee superior mechanical qualities, L-shaped steel pipe concrete columns should have equal limb sections in real engineering design.

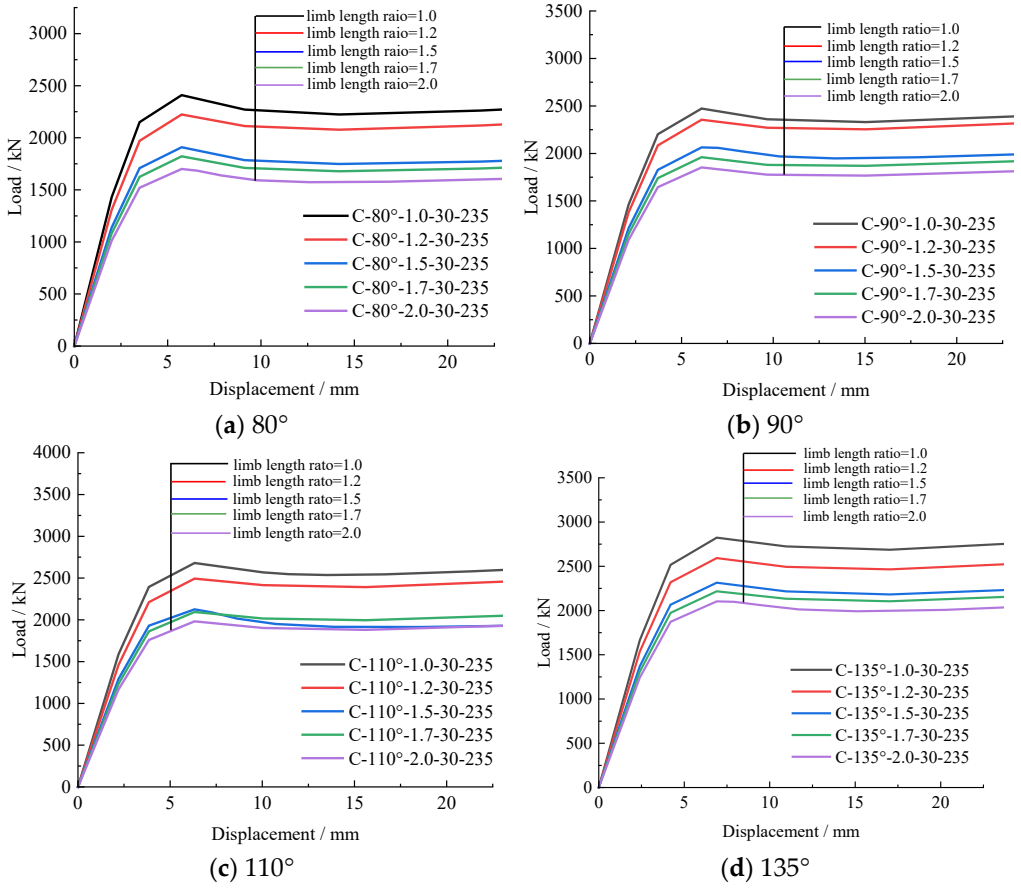


Figure 17. Load–displacement curves of specimens with different length ratios of long limb to short limb.

6.4. Angle between Two Limbs

Figure 18 depicts the impact of the angle between the two limbs on the load–displacement curves of specimens with different limb length ratios. It can be inferred from the figure that specimens with different included angles have similar initial stiffness. The peak bearing capacity of the specimen increases as the included angle grows, as does the peak displacement. The angle between the two limbs has no significant effect on the loss of peak bearing capacity of the specimens.

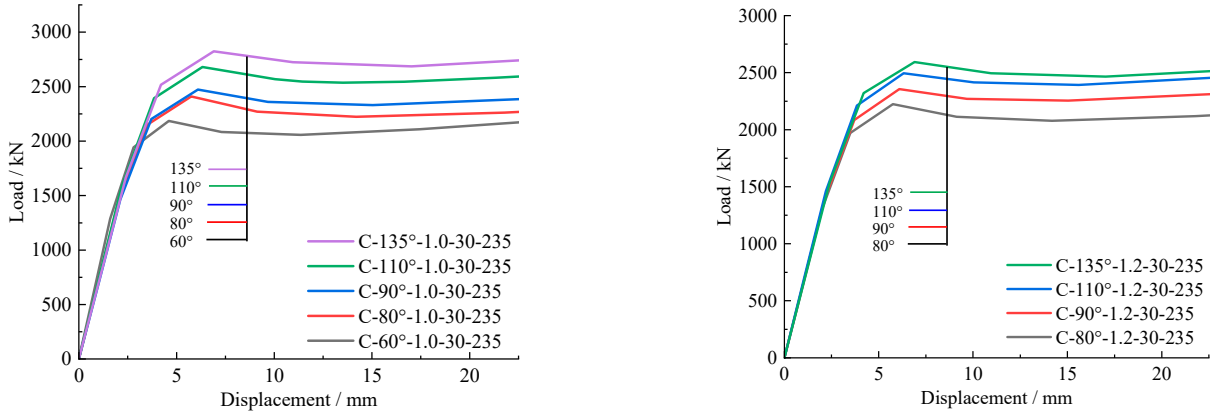
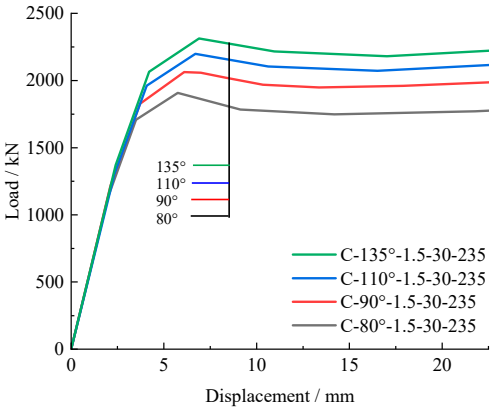
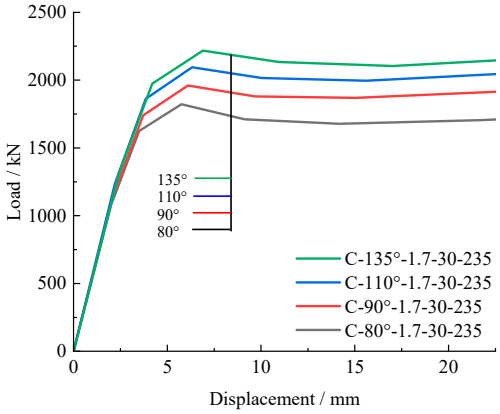


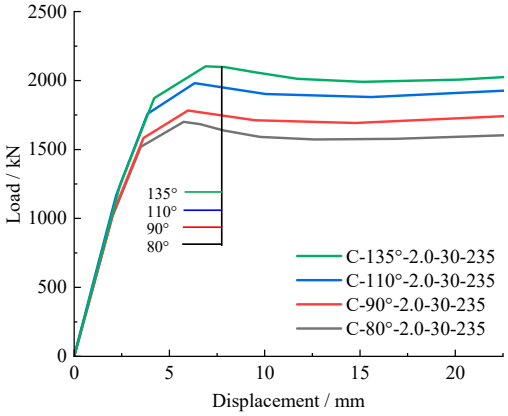
Figure 18. *Cont.*



(**c**) Specimens with a limb length ratio of 1.5



(**d**) Specimens with a limb length ratio of 1.7



(**e**) Specimens with a limb length ratio of 2.0

Figure 18. Load–displacement curves of specimens with different angles between the two limbs.

6.5. Combination Method

Figure 19 displays the load–displacement curves for L-shaped CFST column specimens with different combinations. The figure shows that the F-type specimens have a much larger peak bearing capacity and slightly higher initial stiffness compared to the C-type specimens. This is because the steel pipe in F-type specimens has a stronger constraint effect on concrete, and the F-type specimens are less prone to adverse situations such as weld decay during loading. There is no discernible change in the peak displacement of specimens with different combinations and the rate of peak load reduction.

In order to investigate the sensitivity of the initial stiffness and peak load capacity of L-shaped CFST columns to parameter variations, the data from the above parametric analyses were analyzed in this paper as shown in Table 4. It is worth noting that the change rate of the initial stiffness is calculated as the ratio of the percentage change in the initial stiffness to the percentage change in the parameter. This relative ratio makes it easier to compare the impacts of various parameters quantitatively and consistently.

Table 4. Parameter impact analyses.

Parameter	Rate of Change in Initial Stiffness	Rate of Change in Peak Bearing Capacity
Steel strength	0.12%	64.41%
Concrete strength	17.92%	41.75%
Limb length ratio	−47.40%	−36.80%
Angle between two limbs	−2.63%	34.74%

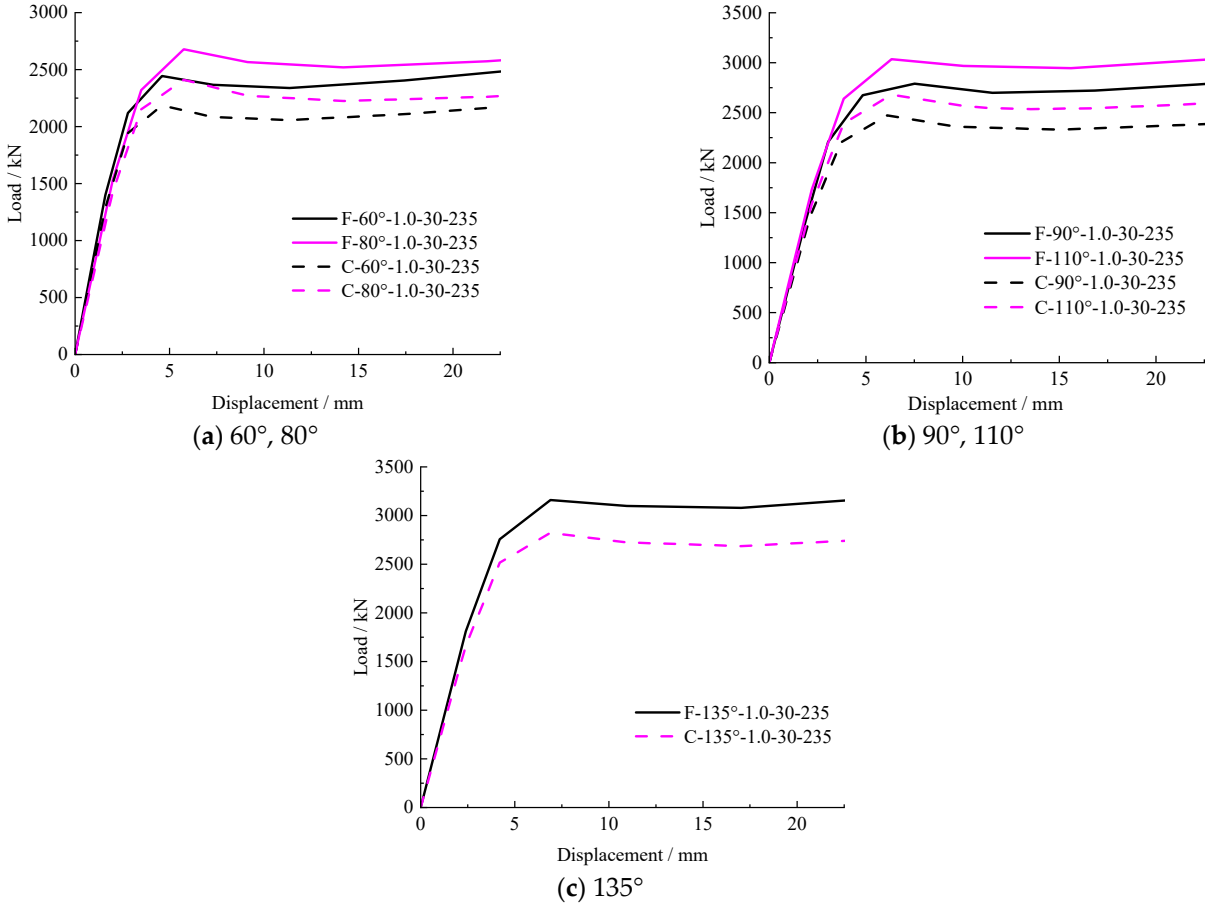


Figure 19. Load–displacement curves of specimens with different combinations.

Table 4 does not include an analysis of changes in combination methods since they are difficult to quantify numerically. Table 4 shows that limb length ratio and steel strength are the two key parameters affecting the initial stiffness and peak bearing capacity of the L-shaped CFST columns. Therefore, in practical engineering design, if the initial stiffness or peak bearing capacity of L-shaped CFST columns needs to be adjusted, priority should be given to changing the limb length ratio of the specimen or the strength of the steel.

7. Conclusions

This study employed ABAQUS to establish finite element models of L-shaped CFST columns with different combinations and compared the calculated results with the test results. The axial compression mechanism of L-shaped CFST columns was investigated in this study through the finite element models. Based on the comprehensive analysis conducted on parameters such as the length ratio of long limb to short limb, the angle between the two limbs, concrete strength, and steel strength, the following conclusions were obtained:

(1) The results obtained through the FEM are in good agreement with the test results in terms of axial compression load–displacement curves and failure modes. The maximum difference between the ultimate bearing capacity results of FEA and testing is 8.7%, with a standard deviation of 0.12, indicating that this modeling method can be used for analyzing the axial compression mechanism of L-shaped CFST columns.

(2) The angle between the two limbs has a significant impact on the stress distribution of concrete and steel pipes. The corner effect increases as the angle between the two limbs decreases. In the elastic–plastic stage, the concrete stress at the internal corner of the specimen with an included angle of 60° increases from 21.92 MPa to 24.00 MPa, and the stress at the external corner increases from 29.25 MPa to 34.14

MPa, and the maximum stress area at the external corner gradually decreases. As for the specimen with an angle of 135°, the stress at the internal corner decreases from 22.22 MPa to 20.53 MPa. The steel pipe stress of the specimen with an angle of 60° concentrates towards the end cavity, while the outer edge of the steel pipe is always in a condition of tensile stress due to the overall bending of the 135° specimen.

(3) In terms of the contact stress between steel pipes and concrete, the combination of F-type specimens can better impose the constraint effect of steel pipes on concrete. The triangular cavity of unequal-limb specimens and specimens with an included angle of 60° cannot effectively exert the interaction between steel pipes and concrete.

(4) The initial stiffness of the L-shaped CFST columns increases by 17.92% with increased concrete strength and decreases by 47.40% with increased limb length ratio. It is not sensitive to changes in steel strength or the angle between the two limbs. The peak bearing capacity increases by 64.41% and 41.75% with increased steel strength and concrete strength, respectively. Compared to C-type and Z-type specimens, the initial stiffness of F-type specimens is slightly higher, and its peak bearing capacity is significantly increased.

(5) L-shaped CFST columns exhibit favorable axial compressive behavior, and their research and engineering applications support the advancement of assembled steel structure residential buildings. In actual projects, F-type equal-limb specimens can be used in priority; for special-angled L-shaped CFST columns, the angle between the two limbs should be considered in terms of the specimen's corner effect and stress distribution, and certain strengthening measures should be taken.

Author Contributions: Conceptualization, Z.T.; Data curation, H.L. and D.H.; Formal analysis, H.L.; Funding acquisition, Z.T.; Investigation, D.H.; Methodology, H.L. and D.H.; Project administration, Z.T.; Resources, Z.T.; Supervision, Z.T.; Validation, H.L.; Visualization, H.L.; Writing—original draft, H.L. and D.H.; Writing—review and editing, Z.T. All authors have read and agreed to the published version of the manuscript.

Funding: This research was funded by the Key Research and Development Programs (Key R and D programs) department of the Science and Technology Department of Yunnan Province, the Faculty of Civil Engineering and Architecture, Kunming University of Science and Technology, number 202003AC100001.

Data Availability Statement: The data supporting this study's findings are available on request from the corresponding author.

Conflicts of Interest: Author Dongji Han was employed by the company 3rd Construction Co., Ltd. of China Construction 5th Engineering Bureau. The remaining authors declare that the research was conducted in the absence of any commercial or financial relationships that could be construed as a potential conflict of interest.

References

1. United Nations Environment Programme. *Emissions Gap Report 2020–Executive Summary: DEW/2310/NA*; UNEP: Nairobi, Kenya, 2020.
2. Hawkins, W.; Cooper, S.; Allen, S.; Roynon, J.; Ibell, T. Embodied carbon assessment using a dynamic climate model: Case-study comparison of a concrete, steel and timber building structure. *Structures* **2021**, *33*, 90–98. [CrossRef]
3. Su, X.; Zhang, X. A detailed analysis of the embodied energy and carbon emissions of steel-construction residential buildings in China. *Energy Build.* **2016**, *119*, 323–330. [CrossRef]
4. Zeitz, A.; Griffin, C.T.; Dusicka, P. Comparing the embodied carbon and energy of a mass timber structure system to typical steel and concrete alternatives for parking garages. *Energy Build.* **2019**, *199*, 126–133. [CrossRef]
5. Song, Z.; Luo, X.; Ge, J. Research on carbon emission in materialization stage of steel structure fabricated residence. *Archit. Technol.* **2023**, *54*, 158–162.
6. Li, Q.; Yue, Q.; Feng, P.; Xie, N.; Liu, Y. Development status and prospect of steel structure industry based on carbon peak and carbon neutrality target. *Prog. Steel Build. Struct.* **2022**, *24*, 1–6+23. [CrossRef]
7. Zong, D. Research on Design of Prefabricated Steel Structure Residence Based on DFMA. Ph.D. Thesis, Chongqing University, Chongqing, China, 2022.
8. Zuo, Z.-L.; Cai, J.; Yang, C.; Chen, Q.-J. Eccentric load behavior of L-shaped CFT stub columns with binding bars. *J. Constr. Steel Res.* **2012**, *72*, 105–118. [CrossRef]

9. Zhou, T.; Chen, Z.; Liu, H. Seismic behavior of special shaped column composed of concrete filled steel tubes. *J. Constr. Steel Res.* **2012**, *75*, 131–141. [CrossRef]
10. Shen, Z.-Y.; Lei, M.; Li, Y.-Q.; Lin, Z.-Y.; Luo, J.-H. Experimental Study on Seismic Behavior of Concrete-Filled L-Shaped Steel Tube Columns. *Adv. Struct. Eng.* **2013**, *16*, 1235–1247. [CrossRef]
11. Zheng, Y.; Yang, S.; Lai, P. Hysteretic behavior of multi-cell L-shaped concrete-filled steel tubular columns at different loading angles. *Eng. Struct.* **2020**, *202*, 109887. [CrossRef]
12. Du, G.; Zhang, J.; Li, Y.; Zhang, J.; Zeng, L. Experimental study on hysteretic model for L-shaped concrete-filled steel tubular column subjected to cyclic loading. *Thin-Walled Struct.* **2019**, *144*, 106278. [CrossRef]
13. Chen, H.; Wang, L.; Chen, H.; Cui, W. Experimental study on the seismic behavior of prefabricated L-shaped concrete-filled steel tube with rectangular multi-cell columns under different lateral loading directions. *J. Constr. Steel Res.* **2021**, *177*, 106480. [CrossRef]
14. Zhang, W.; Chen, Z.; Xiong, Q. Performance of L-shaped columns comprising concrete-filled steel tubes under axial compression. *J. Constr. Steel Res.* **2018**, *145*, 573–590. [CrossRef]
15. Wang, Y.; Guo, L.; Li, H. L-shaped steel-concrete composite columns under axial load: Experiment, simulations and design method. *J. Constr. Steel Res.* **2021**, *185*, 106871. [CrossRef]
16. Wang, Z.; Liu, Z.; Zhou, X.J. Experimental Investigation of Special-Shaped Concrete-Filled Square Steel Tube Composite Columns with Steel Hoops under Axial Loads. *Materials* **2022**, *15*, 4179. [CrossRef]
17. Zhang, L.; Zhang, Y.J.; Tong, J.Z.; Tong, G.S.; Fu, B.; Xu, Y.M. Experimental study on multi-cellular L-shaped CFST slender columns under biaxial eccentric compression. *Structures* **2022**, *45*, 2210–2225. [CrossRef]
18. Zhou, T.; Xu, M.Y.; Chen, Z.H.; Wang, X.D.; Wang, Y.W. Eccentric loading behavior of L-Shaped columns composed of concrete-filled steel tubes. *Adv. Steel Constr.* **2016**, *12*, 227–244. [CrossRef]
19. Zheng, Y.; Zeng, S. Design of L-shaped and T-shaped concrete-filled steel tubular stub columns under axial compression. *Eng. Struct.* **2020**, *207*, 110262. [CrossRef]
20. Lei, M.; Shen, Z.; Li, Y.; Luo, J. Behavior of Concrete-filled T-shaped Steel Tube Intermediate Long Columns Subjected to Axial Loading. *J. Tongji Univ. Nat. Sci.* **2016**, *44*, 520–527.
21. Lei, M.; Shen, Z.; Li, Y.; Luo, J. Sectional Strength of Concrete-filled T-shaped Steel Tube Column Subjected to Axial Compression and Bending Moment. *J. Tongji Univ. Nat. Sci.* **2016**, *44*, 348–354.
22. Lei, M.; Shen, Z.; Li, Y.; Luo, J. Analysis of Behavior of Concrete-filled T-shaped Steel Tube Tall Column Subjected to Uniaxial Eccentric Load. *J. Tongji Univ. Nat. Sci.* **2016**, *44*, 207–212.
23. Liu, X.; Xu, C.; Liu, J.; Yang, Y. Research on special-shaped concrete-filled steel tubular columns under axial compression. *J. Constr. Steel Res.* **2018**, *147*, 203–223. [CrossRef]
24. Liu, J.; Zhou, T.; Lei, Z.; Chen, X.; Chen, Z. Eccentric compression performance of slender L-shaped column composed of concrete-filled steel tubes connected by steel linking plates. *J. Constr. Steel Res.* **2019**, *162*, 105675. [CrossRef]
25. Xiao, Y.; Bie, X.-M.; Song, X.; Zhang, J.; Du, G. Performance of composite L-shaped CFST columns with inner I-shaped steel under axial compression. *J. Constr. Steel Res.* **2020**, *170*, 106138. [CrossRef]
26. Zhang, W.; Li, G.; Xiong, Q.; Gui, H. Seismic behavior of wide-limb special-shaped columns composed of concrete-filled steel tubes. *J. Constr. Steel Res.* **2023**, *205*, 107887. [CrossRef]
27. Chen, X.; Zhou, T.; Chen, Z.; Liu, J.; Jiang, B. Mechanical properties of special-shaped concrete-filled steel tube columns under eccentric compression. *J. Constr. Steel Res.* **2020**, *167*, 105779. [CrossRef]
28. Liu, L.; Tu, Y.; Ye, Y. Finite element analysis of L-shaped concrete filled steel tubular column based on ABAOUS. *J. Shenyang Univ. Technol.* **2011**, *33*, 349–354.
29. Tu, Y.; Wen, Q. Bearing capacity calculation of L-shaped concrete filled steel tubular columns subjected to axial compression. *J. Build. Struct.* **2013**, *34*, 314–320. [CrossRef]
30. Huang, H.; Wang, Y.; Zhang, L.Q.; Chen, M.C.; Zhu, Y.Q. Study on the mechanical behavior of L-shaped concrete-filled steel tubular columns under axial compression. *Struct. Concr.* **2023**, *24*, 2475–2489. [CrossRef]
31. Chen, Z.H.; Xu, J.H.; Zhou, T.; Su, J. Seismic research on column base joint of L-shaped CFST columns under cyclic loading. *Structures* **2022**, *45*, 1212–1224. [CrossRef]
32. Zheng, Y.Q.; Liang, W.G.; Ma, S.S.; Zeng, S.X. Behavior of stiffened and multi-cell L-shaped CFST columns under eccentric compression. *Thin-Walled Struct.* **2022**, *174*, 109156. [CrossRef]
33. Han, L.-H. *Concrete Filled Steel Tubular Structures from Theory to Practice*, 3rd ed.; Science Press: Beijing, China, 2016.
34. Wang, F.-C.; Han, L.-H. Analytical behavior of special-shaped CFST stub columns under axial compression. *Thin-Walled Struct.* **2018**, *129*, 404–417. [CrossRef]
35. Wang, J.; Tian, C. Seismic Behavior Study of 135 Degree Shaped Column. *World Sci-Tech R D* **2013**, *35*, 357–359.

Disclaimer/Publisher's Note: The statements, opinions and data contained in all publications are solely those of the individual author(s) and contributor(s) and not of MDPI and/or the editor(s). MDPI and/or the editor(s) disclaim responsibility for any injury to people or property resulting from any ideas, methods, instructions or products referred to in the content.